

Breathing modulates cortico-hippocampal dynamics during offline states

Nikolaos Karalis

Friedrich Miescher Institute for Biomedical Research <https://orcid.org/0000-0002-1804-9756>

Anton Sirota (✉ sirota@bio.lmu.de)

Ludwig-Maximilians-Universität München <https://orcid.org/0000-0002-4700-6587>

Article

Keywords: breathing, cortico-hippocampal dynamics, offline states, sleep

Posted Date: April 20th, 2021

DOI: <https://doi.org/10.21203/rs.3.rs-296316/v1>

License:   This work is licensed under a Creative Commons Attribution 4.0 International License.

[Read Full License](#)

Breathing modulates cortico-hippocampal dynamics during offline states

Nikolaos Karalis^{1,2,*} and Anton Sirota^{1,*}

¹*Faculty of Medicine, Ludwig-Maximilian University Munich, 82152, Martinsried, Germany*

²*Present address: Friedrich Miescher Institute for Biomedical Research, 4058, Basel, Switzerland*

*Correspondence: nikolaskaralis@gmail.com (N.K.), sirota@bio.lmu.de (A.S.)

Abstract

Network dynamics have been proposed as a mechanistic substrate for the information transfer across cortical and hippocampal circuits. During sleep and offline states, synchronous reactivation across these regions underlies the consolidation of memories. However, little is known about the mechanisms that synchronize and coordinate these processes across widespread brain regions. Here we address the hypothesis that breathing acts as an oscillatory pacemaker, persistently coupling distributed brain circuit dynamics. Using large-scale recordings from seven cortical and subcortical brain regions in quiescent and sleeping mice, we identified a novel global mechanism, termed respiratory corollary discharge, that co-modulates neural activity across these circuits. Analysis of inter-regional population activity and optogenetic perturbations revealed that breathing rhythm couples hippocampal sharp-wave ripples and cortical DOWN/UP state transitions by jointly modulating excitability in these circuits. These results highlight breathing, a perennial brain rhythm, as an oscillatory scaffold for the functional coordination of the limbic circuit, supporting the segregation and integration of information flow across neuronal networks during offline states.

Introduction

1 Over the past century, cortical and subcortical structures of the limbic circuit and the medial temporal lobe have been
2 identified as critical elements of the memory circuit, involved in the formation and retrieval of episodic memories during
3 online states^{85,114} and their consolidation during offline states^{7,13,78}. Despite a growing understanding of local plasticity
4 rules and neural activity correlates, systems-level mechanisms that enable processing and transfer of information across
5 distributed circuits are not well understood.

6 Global, slow neuronal oscillations have been proposed as a mechanism that enables the coordinated interaction between
7 remote brain regions, serving as a source of synchronization in the local circuits and promoting synaptic plasticity^{16,112}.
8 During active behavioral states, sensory-motor integration loops engage widespread circuits and give rise to theta oscilla-
9 tions that entrain local dynamics and provide the substrate for the coordination of the information flow and population
10 coding^{7,15,16,82}. In contrast, during slow-wave sleep, the cortex is in a bistable state, characterized by alternations
11 between generalized silent DOWN, and synchronous UP states across thalamocortical circuits^{7,112,116}, while the hip-
12 pocampal circuits transiently synchronize during sharp-wave bursts associated with high-frequency ripple oscillations¹⁹.
13 These bistable dynamics are pair-wise coordinated^{43,51,95,99,111}, giving rise to emergent spatio-temporal neural pop-
14 ulation dynamics that reactivate awake memory patterns^{34,56,63,90,129}, while their interaction has been postulated to
15 support memory consolidation^{44,73,99,104} and the transfer of memories to their permanent cortical storage^{60,77}.

16 During offline states, systems consolidation across distributed circuits has to rely on the global coupling of internal
17 network dynamics, to enable the coordinated reactivation and cellular consolidation of previous experiences across remote
18 brain regions. However, the mechanisms that support the coherence of such coordinated dynamics across distributed
19 cortical and subcortical circuits during sleep and quiescence remain unknown. From a theoretical perspective, a global
20 pacemaker has been postulated as an effective solution to the coupling of distinct network dynamics^{18,38,61}, but the
21 neural implementation of such a mechanism remains elusive.

22 Here we address the hypothesis that breathing serves as a pacemaker that couples neuronal dynamics across the
23 limbic system during offline states and supports coordinated information flow across cortico-hippocampal circuits.
24 Using multiregional recordings of local field potentials (LFP) and large-scale neural population activity we performed
25 an anatomically-resolved, *in vivo*, functional dissection of the offline state dynamics in the medial prefrontal cortex
26 (mPFC), hippocampus, basolateral amygdala (BLA), nucleus accumbens (NAc), visual cortex, and thalamic nuclei.
27 Using this approach, combined with pharmacological and optogenetic manipulation, we identified an intracerebral cen-
28 trifugal respiratory corollary discharge that mediates the inter-regional synchronization of the limbic circuit and coupling
29 of cortico-hippocampal interaction via correlated excitability modulation.

Results

Respiratory entrainment of prefrontal cortex across brain states

30 To investigate the role of breathing in organizing neuronal dynamics in the mPFC during offline states, we recorded
31 simultaneously the local electrical activity (electroolfactogram; EOG)⁹¹ of the olfactory sensory neurons (OSNs), and
32 single-units and LFP in the mPFC in freely-behaving mice during different vigilance states (**Fig. 1a**). The EOG reflected
33 the respiratory activity and exhibited a reliable phase relationship to the respiratory cycle, as established by comparing
34 this signal to the airflow from the nostrils (**Supplementary Fig. 1a-d**), and was reflected in rhythmic head-motion
35 (**Supplementary Fig. 1b**). We then segmented behavioral states based on the head micro-motion (**Supplementary**
36 **Fig. 1e-f**), differentiating slow-wave sleep (SWS), REM sleep, quiescence, and awake exploration, associated with changes
37 in the breathing frequency (**Fig. 1c**).

38 Both respiratory and the prefrontal LFP signals displayed a prominent spectral peak in the 2-6 Hz range (**Fig. 1b-**
39 **e**), suggesting a potential relationship between these oscillations. The two oscillations were comodulated across a wide
40 frequency range (**Fig. 1f**) and this relationship was preserved throughout many active (online) as well as inactive (offline)
41 states in freely-behaving mice (**Fig. 1c-e; Supplementary Fig. 1g,h**). Coherence and Granger causality analysis of
42 the respiratory and LFP signals suggested that the respiratory oscillation is tightly locked and likely causally involved
43 in the generation of the prefrontal slow-wave LFP oscillation signal during offline states (**Fig. 1g-i; Supplementary**
44 **Fig. 1g,h**).

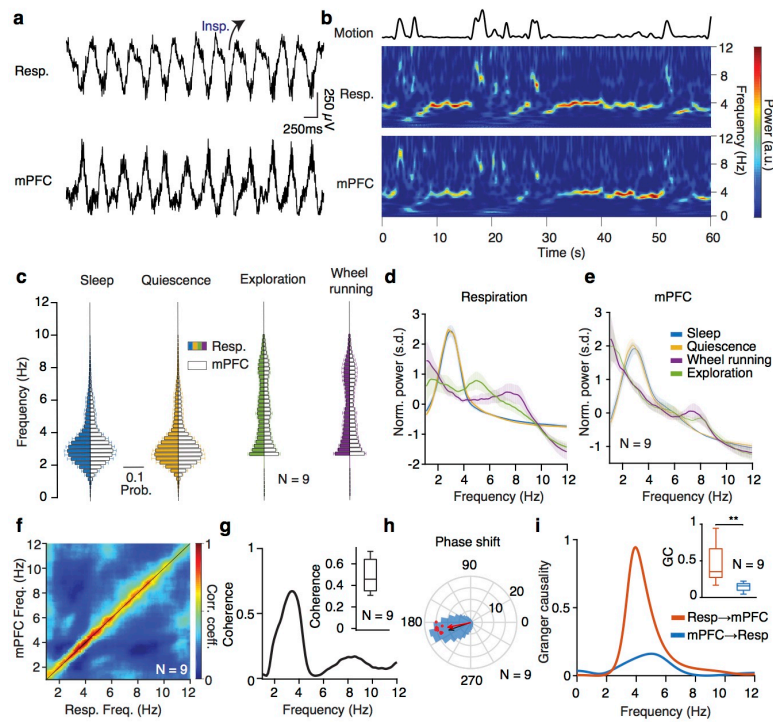


Fig. 1 Prefrontal oscillations are related to breathing throughout behavioral states.

(a) Example traces of simultaneously recorded respiratory EOG and medial prefrontal local field potentials (LFP) (See also Supplementary Fig. 1). (b) Example time-frequency decomposition of respiratory and mPFC LFP signals, revealing the reliable relationship between the two signals. (c) Distribution of peak frequency bins of the spectrally decomposed respiration (left; darker colors) and mPFC LFP (right; lighter colors) during slow-wave sleep, quiescence, exploratory behavior and self-initiated wheel running ($N = 9$ freely-behaving mice) (See also Supplementary Fig. 2). (d,e) Averaged normalized power spectral density of respiration (d) and mPFC LFP (e) across states as in (c). (f) Frequency-resolved comodulation of respiration and mPFC LFP oscillation power, across mice and behaviors ($N = 9$ mice). (g) Example coherence spectrum between respiration and mPFC LFP during offline states. Inset, average coherence value in the 2-5 Hz band ($N = 9$ mice). (h) Phase shift of 2-5 Hz filtered respiration and mPFC LFP signals during offline states for an example animal (blue histogram) and overlaid magnitude of phase modulation ($\log Z$) and average phase shift for all animals (red dots; $N = 9$ mice). Black arrow depicts the average phase and $\log Z$ of the phase shift for the example and the red arrow for the population. (i) Example spectral Granger causality between respiration and mPFC LFP for both causal directions. Inset, group statistics of the average Granger causality for the 4 Hz band (2-5 Hz) between respiration and mPFC LFP for both causality directions ($N = 9$ mice, Wilcoxon signed-rank test, resp \rightarrow mPFC versus mPFC \rightarrow resp, ** $P < 0.01$). a.u., arbitrary units; s.d., standard deviations. Shaded areas, mean \pm SEM.

45 Beyond disengaged offline states, a prominent 4 Hz oscillation is also dominating the mouse mPFC during fear
 46 behavior⁵⁷. The similarity in frequency suggests that breathing is the origin of fear-related 4 Hz oscillations. To explicitly
 47 test this, we exposed mice to auditory, contextual, and innate fear paradigms (**Supplementary Fig. 2a,b**). During
 48 freezing, the respiratory rhythm changed in a stereotypic manner and matched the rhythmic head-motion and the
 49 prefrontal LFP oscillation power, phase, and onset (**Supplementary Fig. 2c-h** **Supplementary Fig. 7j**). Consistent
 50 with the results during offline states, the prefrontal LFP oscillation was coherent with and Granger caused by breathing
 51 (**Supplementary Fig. 2g-h**). Interestingly, the peak breathing frequency was slightly distinct for different types of
 52 fear behavior and the prefrontal peak frequency faithfully matched it, in support of the generality of the described
 53 phenomenon (**Supplementary Fig. 2e**).

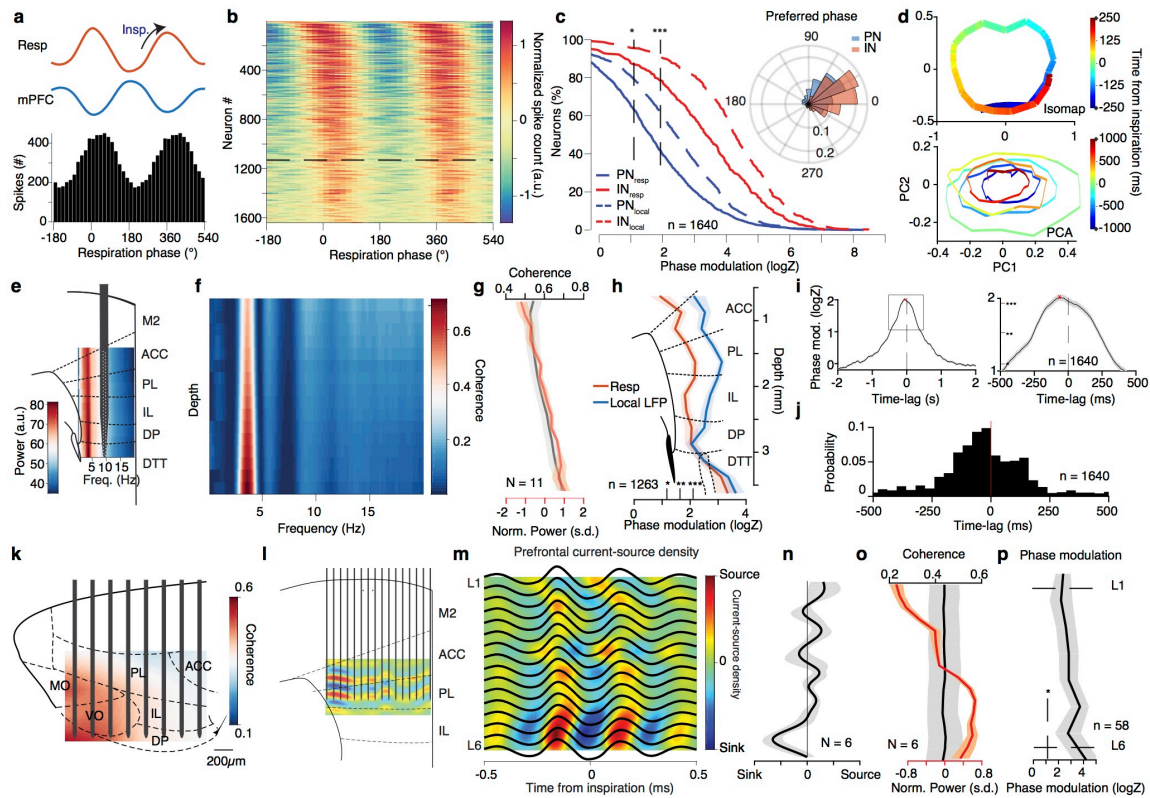


Fig. 2 Topography of prefrontal circuit entrainment by breathing.
 (a) Respiration phase histogram of the spiking activity of an example prefrontal neuron. Top, associated average respiration (red) and mPFC LFP (blue) traces. (b) Color-coded normalized phase histograms of all prefrontal neurons during offline states, ordered by phase modulation magnitude ($n = 1640$ neurons, $N = 13$ freely-behaving and head-fixed mice). The horizontal dashed line indicates the significance threshold for the logZ. (c) Cumulative distribution of the logZ for all prefrontal PNs (blue, $n = 1250$ neurons) and INs (red, $n = 390$ neurons). Phase modulation is assessed in relation to the respiration (solid lines) and the local prefrontal LFP (dashed lines) (See also Supplementary Fig. 3). Inset: Distribution of the preferred phase for PNs (blue) and INs (red). The height of each bar corresponds to the relative number of units. (d) Example trajectory of the mPFC neuronal population activity triggered on the inspiration onset as calculated using Isomap (top) and PCA (bottom) for a longer time window. (e) Schematic depiction of a typical recording using a high-density silicon polytrode inserted in the deep layers of the mPFC, overlaid on an example depth- and frequency-resolved power spectrum spanning all medial prefrontal subregions. (f) Example depth- and frequency-resolved coherence between the respiration and local prefrontal LFP spanning all medial prefrontal subregions. (g) Average depth-resolved normalized power (red) and coherence in the 2-5 Hz band (black) ($N = 11$ head-fixed mice). (h) Depth-resolved average phase modulation statistics (logZ) ($n = 1263$ cells, $N = 11$ mice). (i) Time-lagged phase modulation of prefrontal neuronal population, indicative of directionality from respiration to prefrontal unit activity. Right, the magnified period marked with square. Red stars mark the peak lag ($t = -65$ ms). Horizontal lines indicate levels of significant phase modulation. (j) Distribution of time lag of maximum phase modulation for the population of prefrontal neurons ($n = 1640$ neurons, $N = 13$ mice). (k) Example of 2D coherence between respiration and local LFP throughout the frontal subregions. (l) Schematic depiction of a 16-shank probe ($50\mu\text{m}$ shank spacing) inserted in the prelimbic region of the mPFC to record simultaneously from all cortical layers and an example inspiration-triggered current-source density profile. (m) Example average inspiration-triggered LFP traces and overlaid corresponding translaminar current-source density profile from the dorsal mPFC. (n) Average inspiration-triggered translaminar normalized current-source density profile from the dorsal mPFC ($N = 6$ head-fixed mice). (o) Average cortical layer-resolved profile of the normalized 2-5 Hz band local LFP power (red) and coherence with respiration (coherence) ($N = 6$ mice). (p) Cortical layer-resolved unit phase modulation statistics (logZ) ($n = 58$ cells, $N = 6$ mice). Shaded areas, mean \pm SEM, a.u., arbitrary units; s.d., standard deviations; L1, layer 1; L6, layer 6. Stars indicate significance levels (* $P < 0.05$; ** $P < 0.01$; *** $P < 0.001$).

Having established the generality of the coupling between breathing and LFP oscillation in the mPFC across distinct states, consistent with previous reports^{9,83,133}, we focused on the enigmatic and least understood quiescence and slow-wave sleep states. Slow waves in cortical LFP during offline states are linked to the thalamocortical slow oscillation^{112,116},

57 therefore the dominance of the respiratory rhythm on the prefrontal LFP warrants careful examination of the role of
58 respiration in offline state dynamics. To this end we performed large-scale recordings of LFP and population unit activity
84 across multiple brain regions in head-fixed mice during quiescence state.

85 To further investigate the extent of respiratory entrainment of prefrontal circuits at the level of neural population
86 activity, we examined the firing of extracellularly recorded single neurons in mPFC in relation to the respiratory phase
87 (**Fig. 2a**). We observed that $\sim 60\%$ of putative prefrontal principal cells (PN) and $\sim 90\%$ of putative inhibitory interneu-
88 rons (IN), identified based on their extracellular waveform features⁶ (**Supplementary Fig. 3a,b**), were significantly
89 modulated by the phase of breathing cycle (**Fig. 2b,c; Supplementary Fig. 3c**) and more strongly modulated by the
90 past phase of the respiratory cycle (**Fig. 2i,j**). Most modulated cells fired preferentially in the trough/ascending phase
91 of the local oscillation, corresponding to the inhalation phase (**Fig. 2b,c; Supplementary Fig. 3d**), largely indepen-
92 dently of the ongoing breathing cycle duration (**Supplementary Fig. 3g**), and are even more strongly modulated by
93 the phase of the local oscillation (**Fig. 2c; Supplementary Fig. 3e,f**). To ensure that this modulation is not a result
94 of mechanical stimulation of the neurons due to breathing-related brain pulsation in relation to the electrode, we posited
95 that such an artifact would be expected to be most severe for neurons located closer to the electrode, as they would
96 be more likely to be mechanically stimulated. However, we did not find a correlation between modulation strength and
97 distance to the electrode inferred from the amplitude of the action potential or any modulation of the unit amplitude by
98 the respiratory phase (**Supplementary Fig. 3i-l**).

99 In order to characterize the effect of this respiratory entrainment on prefrontal population dynamics, we performed
100 dimensionality-reduction (Isomap and PCA) on the correlation matrix of inspiration-triggered unit activity. Using this
101 approach, we identified that breathing entrains prefrontal population activity in a low-dimensional, periodic orbit, thus
102 exhibiting cyclic attractor characteristics, whereby population dynamics would remain stable across consecutive breathing
103 cycles (**Fig. 2d; Supplementary Fig. 4c,d**).

Topography of respiratory entrainment

104 mPFC consists of multiple subregions along the dorsoventral axis, all of which are characterized by differential afferent and
105 efferent connectivity and behavioral correlates^{49,50}. To understand the origin and anatomical substrate of the respiratory
106 entrainment of prefrontal circuits, we performed a three-dimensional trans-laminar and trans-regional characterization
107 of the mPFC field potentials using custom-designed high-density silicon probes in freely-behaving and head-fixed mice
108 (**Fig. 2e-p; Supplementary Fig. 4e**). These recordings revealed a consistent increase from dorsal to ventral mPFC in
109 both the power of the breathing-related oscillation and its coherence with breathing (**Fig. 2e-g**). Similarly, the coherence
110 was stronger in the anterior prefrontal regions (**Fig. 2k**).

111 The presence of an oscillation in the mPFC with this particular profile could also be consistent with a volume-conducted
112 signal from the high amplitude field potentials generated by bulbar dipoles; since olfactory bulb (OB) LFP is dominated
113 by breathing-related oscillations^{2,42,72}. Further, the multitude of refferent pathways to the prefrontal cortex originating
114 in the OB and their complex 3D axonal termination patterns, combined with the spatio-temporal superposition of

115 multiple laminae-specific dipoles and the volume conduction from distant sites make the exact interpretation of LFP
116 patterns alone challenging. To distinguish these potential sources of origin and identify local current dipoles that might
117 underlie observed prefrontal LFP patterns, we recorded LFP activity across the prefrontal cortical layers and calculated
118 the current-source density (CSD) (**Fig. 2l-n; Supplementary Fig. 4b**). This analysis revealed a prominent pattern of
119 sinks in the deep cortical layers at the inspiration phase, giving rise to an increased LFP power and unit-LFP coupling
120 in the deep layers (**Fig. 2o,p**), weighing against the hypothesis of volume conduction and suggestive of a synaptic origin
121 of the prefrontal LFP oscillation. To further control for the possibility of strong volume conducted signals affecting the
122 recorded and calculated signals, we constructed a simple model of ventral or lateral oscillatory sources that volume
123 conduct to the recorded region. In both these cases, the model failed to account for the experimentally observed LFP
124 and CSD patterns (**Supplementary Fig. 4a**).

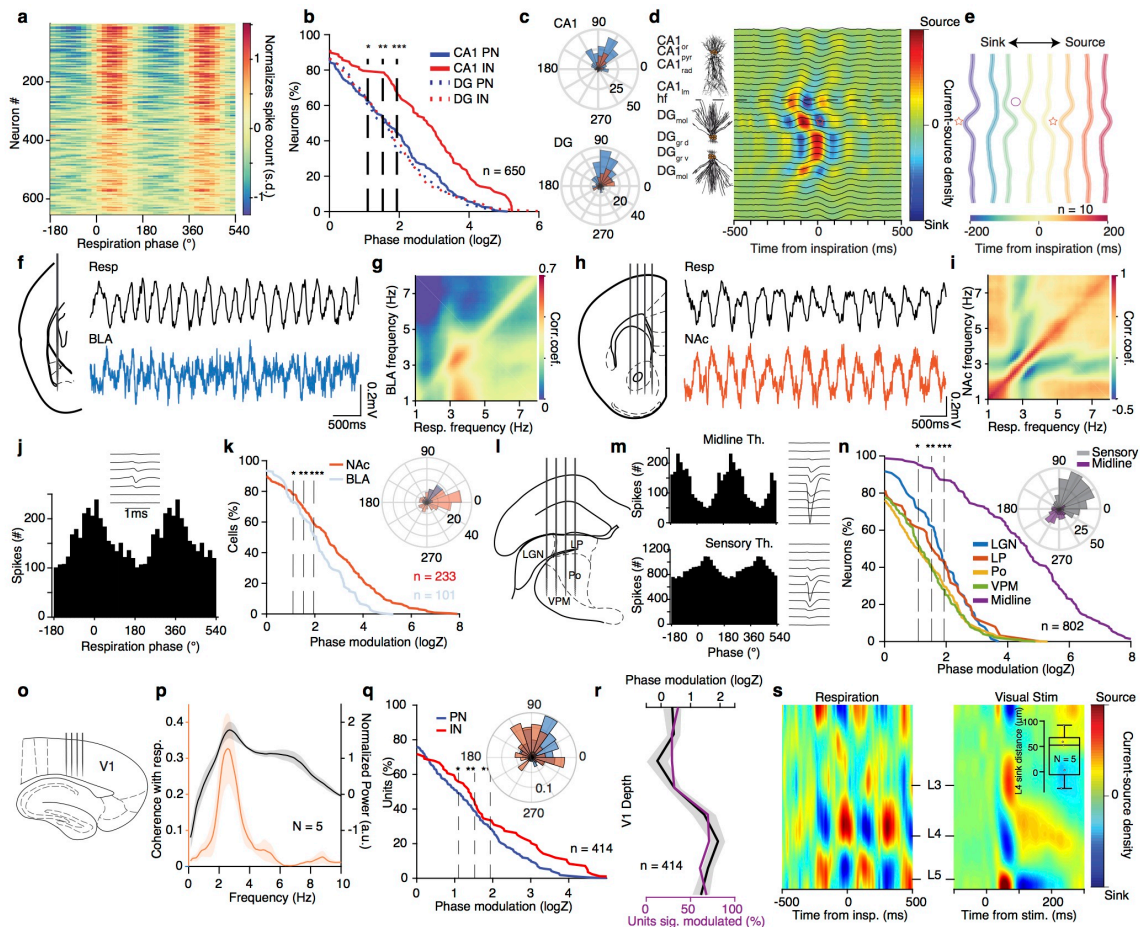
125 Harnessing the advantages of spatial information from the silicon probe recordings, we characterized the entrainment
126 of single units across prefrontal subregions and cortical layers. Although cells were phase-modulated throughout the
127 prefrontal subregions, the average modulation strength was increased as a function of distance from the dorsal surface
128 (**Fig. 2h; Supplementary Fig. 3e,f**). These results, given the increased density of polysynaptic projections from the
129 OB to ventral mPFC subregions⁸³, suggest that the bulbar refferent input to the mPFC is giving rise to the observed
130 LFP signals. Rhythmic airflow could entrain the olfactory sensory neurons (OSNs), that are known to respond both to
131 odors and mechanical stimuli⁴⁶, and propagate through the olfactory bulb and the olfactory system to the prefrontal
132 region. To understand the potential role of breathing in orchestrating the hippocampo-cortical dialogue, we undertook
133 a detailed investigation of the mechanism and tested for a possible modulatory role of the breathing rhythm on brain
134 circuits.

Widespread respiratory modulation of limbic circuits during offline states

135 Given the prominent modulation of mPFC by breathing, we hypothesized that concurrent entrainment of other regions
136 could be underlying their generalized long-range interaction, as has been suggested before for theta oscillations during
137 active states^{17,82}. For this, we turned our attention to other brain regions, reciprocally connected to the mPFC, that are
138 known to interact with prefrontal networks in different behaviors and be involved in memory consolidation^{14,43,94}.

139 In the dorsal hippocampus, ~60% of both CA1 PNs and INs and dentate gyrus (DG) PNs and 80% of CA1 INs
140 were modulated by the phase of breathing, firing preferentially after the inspiration (**Fig. 3a-c**), in line with previous
141 reports of respiratory entrainment of hippocampal activity during immobility and anesthesia^{68,87,125,133}. A separation of
142 CA1 PNs based on their relative position within the pyramidal layer into populations with known distinct connectivity
143 patterns^{81,124} did not reveal particular differences in their modulation by breathing, suggesting a generality of this
144 entrainment throughout the CA1 sub-populations (**Supplementary Fig. 5d**).

145 To understand what afferent pathways are responsible for breathing-related synaptic currents that underlie the modu-
146 lation of spiking activity, we calculated the finely-resolved (23 μ m resolution) laminar profile of inspiration-triggered dorsal



154
 155 **Fig. 3 Breathing modulates hippocampal, thalamic, BLA, NAc, and V1 neuronal activity.**
 156 (a) Color-coded respiration phase histograms of the normalized firing rate of all hippocampal cells (n = 650 cells). (b) Cumulative
 157 distribution of the modulation strength by respiration phase for all CA1 and DG PNs (CA1, n = 226 cells; DG, n = 206 cells; N = 22
 158 mice) and INs (CA1, n = 98 cells; DG, n = 120 cells). (c) Distribution of the preferred phase for all significantly phase-modulated
 159 CA1 (top) and DG (bottom) cells. (d) Schematic depiction of CA1 pyramidal and DG granular cell somatodendritic domains
 160 aligned to the example inspiration-triggered high-density CSD profile of the dorsal hippocampus. Horizontal dashed line indicates
 161 the hippocampal fissure (See also Supplementary Fig. 5 for interpretation). (e) Average normalized inspiration-triggered CSD
 162 profile of dorsal hippocampus at different lags from inspiration (N = 10 head-fixed mice). Stars mark the middle molecular layer
 163 sink and circles the outer molecular layer sink (f, h) Left, schematic of recording configurations. Right, example simultaneously
 164 recorded respiration and BLA (f) or NAc (h) LFP trace. (g, i) Example frequency-resolved comodulation of respiration and BLA
 165 (g) or NAc (i) LFP oscillation power. (j) Respiration phase histogram of the spiking activity of one example NAc neuron. Inset, the
 166 spatio-temporal spike waveform for the respective units. (k) Cumulative distribution of the logZ for all BLA (blue) or NAc (red) cells
 167 (BLA: n = 101 cells, NAc: n = 233 cells). Inset, distribution of the mean preferred respiration phases of all significantly modulated
 168 cells. (l) Schematic of recording configuration for sensory thalamus. (m) Respiration phase histograms of the spiking activity
 169 (left) and spatio-temporal spike waveforms of respective example units from the midline (top) and sensory (bottom) thalamus.
 170 (n) Cumulative distribution of the modulation strength for all thalamic neurons (n=802 cells). Inset, distribution of the preferred
 171 phase for all significantly phase-modulated sensory and midline thalamic cells. (o) Schematic of recording configuration for V1. (p)
 172 Spectral V1 LFP power and coherence with respiration. (q) Cumulative distribution of the modulation strength by the respiration
 173 phase for all V1 PNs and INs. Inset, distribution of the preferred respiration phase for all significantly phase modulated neurons.
 174 (r) Cortical depth-resolved phase modulation magnitude and cell percentage. (s) Example inspiration-triggered high-density CSD
 175 profile of V1, compared with the CSD profile triggered by visual stimulation. Inset, spatial distance between L4 sinks for respiration-
 and visual stimulation-triggered CSD. Stars indicate significant phase modulation levels (* P<0.05; ** P<0.01; *** P<0.001).

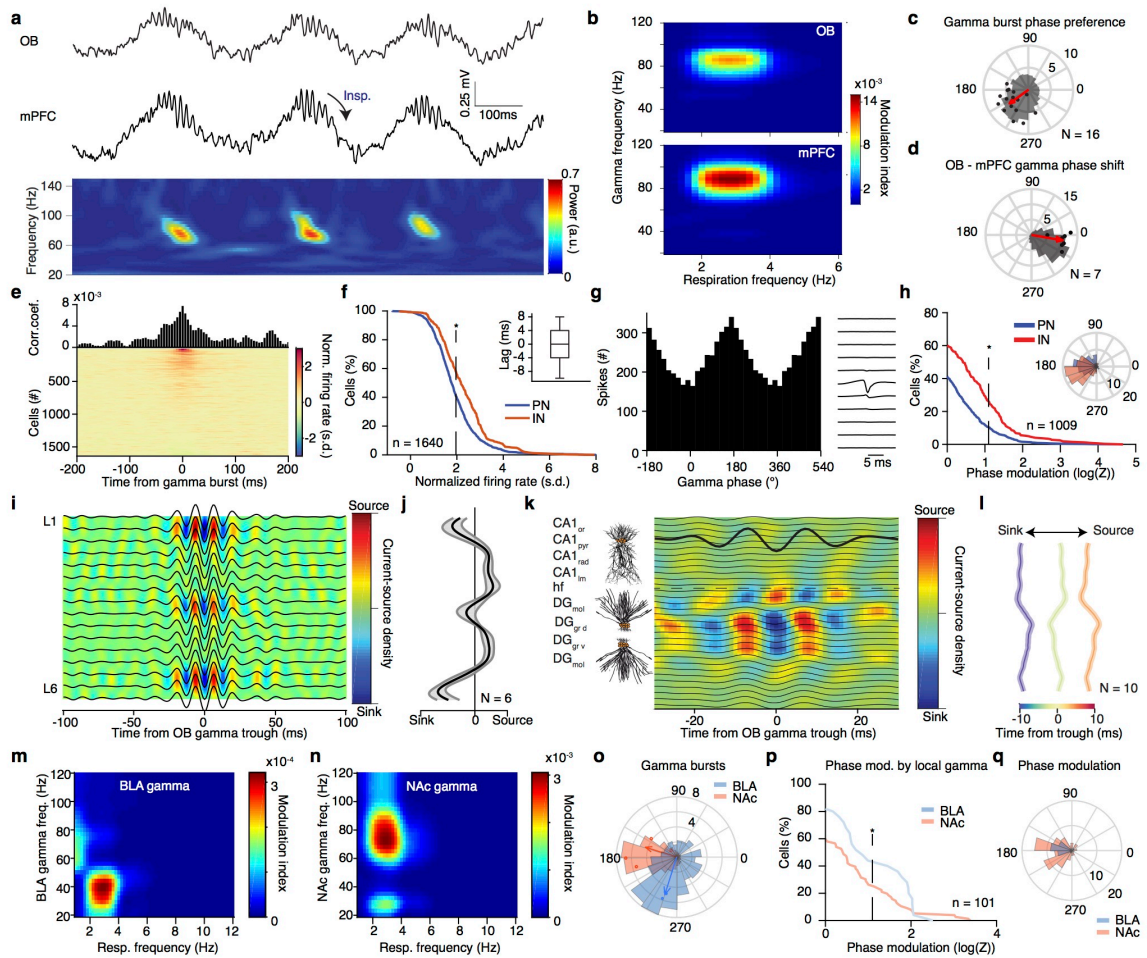
147 hippocampal CSD, enabling the identification of synaptic inputs into dendritic sub-compartments. Although the LFP

148 profile only highlights the prominence of the respiratory band in the DG hilus region (**Supplementary Fig. 5a**), depth-
149 resolved coherence analysis identifies coherence with breathing in the dendritic CA1 and DG layers(**Supplementary**
150 **Fig. 5b,c**), while high-resolution CSD analysis revealed more accurately the presence of two distinct and time-shifted
151 respiratory-related inputs to DG dendritic sub-compartments (**Fig. 3d,e; Supplementary Fig. 5e**). Inspiration was
152 associated with an early sink in the outer molecular layer of DG, indicative of input from the layer II (LII) of the lateral
153 entorhinal cortex (LEC), followed by a sink in the middle molecular layer of DG, indicative of input from the layer II of
176 the medial entorhinal cortex (MEC) (**Fig. 3d,e; Supplementary Fig. 5e**).

177 To explore the extent of cortical and subcortical entrainment by breathing, we further recorded LFP and single-unit
178 activity in the BLA, NAc, V1, as well as somatic and midline thalamus (**Fig. 3f-s; Supplementary Fig. 4e**). Similar to
179 mPFC, LFP in both BLA and NAc was comodulated with breathing across a range of frequencies, with most prominent
180 modulation at ~ 4 Hz, the main mode of breathing frequency during quiescence (**Fig. 3f-i**), and exhibited reliable cycle-
181 to-cycle phase relationship with the respiratory oscillation (**Supplementary Fig. 6a,b**). Given the nuclear nature and
182 lack of lamination of these structures, which obfuscates the interpretation of slow LFP oscillations, we examined the
183 modulation of single-unit activity by the phase of breathing, revealing that a large proportion of BLA, NAc, and thalamic
184 neurons were significantly modulated by respiration, notably firing in distinct phases of the breathing cycle (**Fig. 3j-n**).
185 In the visual cortex, both LFPs (**Fig. 3p**) and a large fraction of neurons (**Fig. 3q**) were phase-modulated by breathing.
186 Interestingly, the magnitude of phase modulation was maximal in layers 4-6, which is consistent with both the phase
187 modulation of sensory thalamic neurons (**Fig. 3r**), the presence of strong coherence of the LFP with respiration in the
188 thalamus (**Supplementary Fig. 5b**) and respiration-related CSD sinks in the L4/5 where thalamic inputs arrive (**Fig.**
189 **3s**).

Reafferent origin of limbic gamma oscillations

190 A prominent feature of prefrontal LFP is the presence of fast gamma oscillations (~ 80 Hz), believed to emerge due to local
191 synchronization^{113,118} (**Fig. 4a**). To investigate the relationship of prefrontal gamma oscillations to the breathing rhythm
192 and well-known OB gamma oscillations^{3,40,42,66}, we recorded simultaneously from the two structures and calculated the
193 phase-amplitude coupling between breathing and gamma oscillations (**Fig. 4a,b; Supplementary Fig. 6c,d**). Both
194 OB and mPFC fast gamma oscillations were modulated by the phase of breathing, such that gamma bursts occurred
195 predominantly simultaneously and in the descending phase of the local LFP (**Fig. 4c**). The simultaneously occurring
196 OB and mPFC gamma oscillations matched in frequency and exhibited a reliable phase relationship with a phase lag
197 that suggests directionality from the OB to the mPFC (**Fig. 4d; Supplementary Fig. 6d**). To examine the underlying
198 synaptic inputs mediating the occurrence of these oscillations in the mPFC, we calculated CSD across mPFC layers,
199 triggered on the phase of the OB gamma bursts. This analysis revealed a discrete set of sinks across prefrontal layers
200 associated with OB bursts (**Fig. 4i,j**). Similar to the slow time scale LFP signals, these results suggest that fast gamma



203

204 **Fig. 4 Reafferent gamma entrainment of limbic circuits.**

205 (A) Example simultaneously recorded LFP traces (top) from OB and mPFC LFP and the spectral decomposition of mPFC LFP
 206 in the gamma range (bottom). (b) Color-coded modulation strength of OB (top) and mPFC (bottom) gamma power by respiration
 207 phase for an example animal. (c) Phase distribution of mPFC gamma bursts for an example animal (gray histogram) and average
 208 preferred phase and phase modulation strength (logZ) for all animals (N = 16 freely-behaving and head-fixed mice). The red arrow
 209 indicates the population average preferred phase and log(Z). (d) Distribution of the phase shift between OB and mPFC gamma
 210 filtered traces for one example animal (gray histogram) and average phase shift and phase-coupling strength (log(Z), red dots)
 211 for all animals (N = 7 mice) (See also Supplementary Fig. 6). (e) Gamma-burst triggered time histogram for one example mPFC cell
 212 and color-coded normalized time histograms for all mPFC cells (n = 1640 cells). (f) Cumulative distribution of the gamma-triggered
 213 normalized firing of mPFC PNs (n = 1250 cells) and INs (n = 390 cells). Inset, time-lag between time from gamma burst and
 214 peak firing probability for all significantly responsive cells. (g) Gamma phase histogram of one example mPFC unit (left) and the
 215 respective unit spike spatio-temporal waveform (right). (h) Cumulative distribution of the modulation strength (logZ) for all PNs
 216 (blue, n = 685 neurons) and INs (red, n = 324 neurons). Phase modulation is assessed in relation to the phase of the locally recorded
 217 prefrontal gamma oscillation. Inset, distribution of the mean preferred phases of all significantly modulated PN and IN cells. (i, j)
 218 Example (i) and average zero-lag (j) OB gamma-triggered translaminal CSD of the dorsal mPFC LFP profile. (N = 6 head-fixed
 219 mice). (k) Example OB gamma-triggered CSD profile of dorsal hippocampus. Horizontal dashed line indicates the hippocampal
 220 fissure. (l) Average normalized OB-triggered current-source density profile of the dorsal hippocampus at different time lags from
 221 OB gamma trough (N = 10 head-fixed mice). (m, n) Example phase-power modulation of BLA (m) and NAc (n) gamma activity
 222 by respiration. (o) Example distribution of the respiratory phase of BLA and NAc gamma bursts (histogram) and mean preferred
 223 phase of gamma occurrence and modulation strength (dots; BLA, blue, N = 3 head-fixed mice; NAc, red, N = 4 head-fixed mice).
 224 (p) Cumulative distribution of modulation strength for local gamma phase entrainment of spikes of all BLA (blue, n = 25 cells)
 225 and NAc cells (red, n = 76 cells). (q) Distribution of the mean preferred gamma phase for each significantly modulated BLA and
 NAc cell. Star indicates significance (* P<0.05). Shaded areas, mean ± SEM.

201 oscillatory signals in mPFC are generated by OB-gamma rhythmic polysynaptic inputs to mPFC and are not exclusively
202 attributable to a locally generated rhythm.

226 Examination of the OB ~ 80 Hz gamma-triggered dorsal hippocampal CSD revealed a DG outer molecular layer sink
227 (**Fig. 4k,l**), a profile distinct from the similar frequency $CA1_{lm}$ gamma (**Supplementary Fig. 6e**). This would be
228 consistent LEC LII inputs, a region known to exhibit olfactory-related activity⁶⁴. In parallel, slow BLA gamma (~ 40
229 Hz) and fast NAc gamma (~ 80 Hz) oscillations were modulated by the phase of breathing, occurring predominantly in
230 the trough and ascending phase of breathing respectively (**Fig. 4m-o**).

231 To examine whether these breathing-modulated OB-mediated gamma oscillations have a functional role in driving
232 local neuronal activity, we quantified coupling of local single units to mPFC gamma signals, revealing that $\sim 40\%$ of
233 principal cells and $\sim 55\%$ of interneurons increased their firing rate in response to local gamma oscillations (**Fig. 4e,f**).
234 Interestingly, $\sim 10\%$ of PN and $\sim 30\%$ of IN were significantly phase modulated by gamma oscillations, firing preferentially
235 in the trough of the local oscillation (**Fig. 4g,h**). Similarly, $\sim 40\%$ of BLA and $\sim 25\%$ of NAc cells fired preferentially in the
236 trough of the local gamma oscillations (**Fig. 4p; Supplementary Fig. 6f,g**), suggesting the fine-timescale modulation
237 of downstream regions by OB gamma oscillations.

Efferent and reafferent mechanisms of respiratory entrainment

238 These results suggest a mechanistic picture in which the OB reafferent gamma and respiration-locked slow time scale
239 currents are responsible for the observed breathing-associated LFP patterns in the mPFC, consistent with disruption
240 of these LFP patterns after OB lesion or tracheotomy^{9,53,83,123}. However, the distributed, phase-specific and massive
241 modulatory effect that breathing had on unit activity across wide brain regions is at odds with the anatomically-specific
242 synaptic pathways that we identified as responsible for slow and fast currents.

243 To causally test whether OB reafferent input is the sole origin of the LFP patterns and unit entrainment, we employed
244 a pharmacological approach, that enables selective removal of the reafferent input. A well-characterized effect of systemic
245 methimazole injection is the ablation of the olfactory epithelium (**Supplementary Fig. 7a**) that hosts the olfactory
246 sensory neurons⁸, that respond to both odors and mechanical stimuli⁴⁶. Effectively, this deprives the OB of olfactory and
247 respiratory input, while leaving the breathing rhythm generators (**Supplementary Fig. 7b-e**), as well as the bulbar
248 circuits intact, enabling us to study the contribution of re-afferent input on the brain activity in freely-behaving mice.
249 This manipulation eliminated the respiration-coherent and spectrally-narrow prefrontal slow oscillatory LFP component
250 (**Fig. 5a-d; Supplementary Fig. 7g-h**), consistent with the disappearance of the CSD sink in deep layers (**Fig. 5e**),
251 while at the same time abolishing the olfactory-related prefrontal gamma oscillations (**Fig. 5f,g**), without altering the
252 respiratory dynamics (**Supplementary Fig. 7b-e**). These results confirm the hypothesis that a respiratory olfactory
253 reafference (ROR) is responsible for the rhythmic cortical LFP during offline states, as suggested previously for other
254 states^{9,53,83,123}.

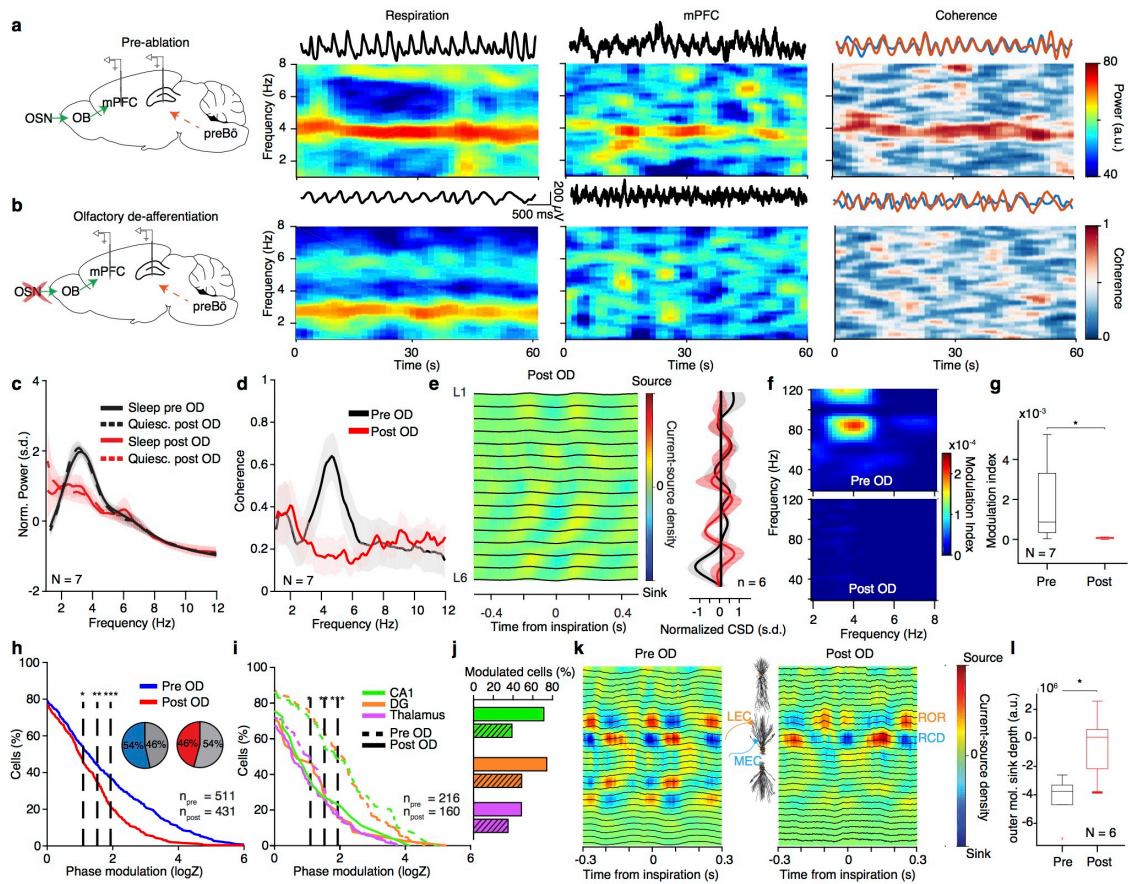


Fig. 5 Reafferent respiratory input accounts for LFP but not neuronal entrainment.

(a,b) Left, schematic of the manipulation strategy. Right, example time-frequency decomposition of power and coherence between respiratory and mPFC LFP signals during quiescence before (a) and after (b) OD. (c) Average normalized mPFC power spectra before and after OD (N = 7 head-fixed mice). (d) Coherence spectrum between respiration and mPFC LFP before and after OD (N = 7 mice). (e) Left, example inspiration-triggered CSD of the mPFC LFP during quiescence and sleep after OD. Right, average normalized CSD at zero lag (N = 6 mice) (See also Supplementary Fig. 7). (f) Example power-phase modulation of mPFC gamma oscillations before (top) and after (bottom) OD. (g) Average mPFC power-phase modulation strength of ~80 Hz gamma oscillations (N = 7 mice; paired t-test: before vs. after OD). (h) Cumulative distribution of modulation strength for all mPFC neurons pre and post OD (Pre: n = 511 cells; Post: n = 431 cells). Inset, percentage of significantly phase-modulated cells before and after OD. (i) Cumulative distribution of modulation strength for CA1, DG, and somatic thalamus neurons before and after OD. (j) Percentage of significantly phase-modulated cells before and after OD. (k) Example inspiration-triggered CSD of the dorsal hippocampus LFP before (left) and after (right) OD. (l) Average outer molecular layer sink depth (N = 6 head-fixed mice; paired t-test: before vs. after OD). Shaded areas, mean ± SEM a.u., arbitrary units; s.d., standard deviations; n.s., not significant. Stars indicate significance levels (* P<0.05; ** P<0.01; *** P<0.001). s.d., standard deviations; a.u., arbitrary units; OD, olfactory deafferentation.

255 Surprisingly, the olfactory deafferentation (OD) left most prefrontal and thalamic neurons modulated by breathing,
 256 although the strength of modulation was reduced (Fig. 5h,i), suggesting that a so-far undescribed and yet-to-be-
 257 determined anatomical-physiological mechanism of centrifugal efference copy provided by brainstem circuits (termed
 258 ascending respiratory corollary discharge (RCD)) is responsible for the massive entrainment of limbic neurons. Interest-
 259 ingly, following OD, mice exhibited intact memory and fear expression, suggesting that the RCD might be underlying
 260 the behavioral expression (Supplementary Fig. 7i-k). Dorsal hippocampal neurons were somewhat stronger affected
 261 by the ablation, yet more than 40% of cells were still significantly phase modulated by breathing (Fig. 5i,j), indicating a
 262 differential degree of contribution of RCD and ROR to unit firing across mPFC, hippocampus, and thalamus. In contrast

263 to the prefrontal CSD, the olfactory deafferentation led to a strong reduction of the outer molecular layer current-sink
264 originating in LEC LII in the respiration-locked CSD (**Fig. 5k,l**), while leaving MEC LII sink and other non-respiration
265 related CSD patterns intact (**Supplementary Fig. 7h**), suggesting that the LEC input is driven by ROR, while MEC
266 input is driven by RCD.

Hippocampal network dynamics are modulated by breathing

267 From the results so far, it is clear that hippocampal neuronal activity during offline states is massively modulated by
268 breathing, in part via afferent entorhinal inputs to the DG. However, during quiescence and slow-wave sleep, hippocampal
269 activity is characterized by recurring nonlinear population events such as sharp-wave ripple (SWR) complexes and dentate
270 spikes (DS), that organize the local spatio-temporal population activity implicated in the replay of memories⁹⁰ and known
271 to be tightly temporally correlated with slow cortical oscillations during sleep¹¹².

272 During CA1 ripples (**Fig. 6a-c; Supplementary Fig. 8a**)²¹, CA1 PN and IN, and to a lesser extent DG cells, were
273 strongly (**Fig. 6e**) and rhythmically (**Fig. 6d**) activated. Ripple occurrence was strongly modulated by breathing⁶⁷,
274 biased towards the post-inspiratory phase, while ripples were suppressed during exhalation (**Fig. 6f-g**). Following olfac-
275 tory deafferentation, ripples remained significantly phase modulated by breathing (**Fig. 6h**), suggesting that RCD is the
276 main source of their modulation. Keeping up with the role of the entorhinal input in mediating respiratory drive on rip-
277 ples, we observed a consistent relationship between the magnitude of MEC LII sink directly preceding ripple occurrence
278 and the phase within the respiratory cycle of the ripple occurrence (**Supplementary Fig. 8c,d**).

279 Another prominent hippocampal offline state-associated pattern are dentate spikes, defined as large positive potentials
280 in the DG hilus region¹⁰, which are believed to occur in response to strong inputs in the molecular layer, such as during
281 entorhinal UP states (**Supplementary Fig. 5e-f**)^{51,119}. During DS, both DG (~70% PN and IN), CA1 (~40% PN and
282 ~70% IN), and mPFC (~40% PN and ~70% IN) cells were strongly excited (**Supplementary Fig. 5g**). Consistent
283 with respiratory entrainment of the entorhinal inputs, the occurrence of DS was strongly modulated by the breathing
284 phase, both before and after OD, with the majority of events occurring after inspiration (**Supplementary Fig. 5h-j**).

Breathing organizes prefrontal UP states and hippocampal output

285 Similar to the hippocampus, during quiescence and slow-wave sleep neocortical circuits exhibit nonlinear bistable dynam-
286 ics in the form of DOWN and UP states. We posited that the strong rate of modulation of prefrontal neural activity by
287 breathing would bias these dynamics. To test this prediction, we identified prefrontal UP and DOWN states based on
288 the large-scale population activity and characterized their relationship with the phase of the ongoing breathing rhythm
289 (**Fig. 6i**). Both UP and DOWN state onsets were strongly modulated by the breathing phase and time from inspiration
290 (**Fig. 6j-m**), while the magnitude of modulated UP states followed the profile of UP state onset probability (**Fig. 6k**).
291 In line with the results on ripples and prefrontal units, UP and DOWN state modulation was not affected by olfactory
292 deafferentation, suggesting that RCD is the source of this modulation (**Fig. 6m,n**).

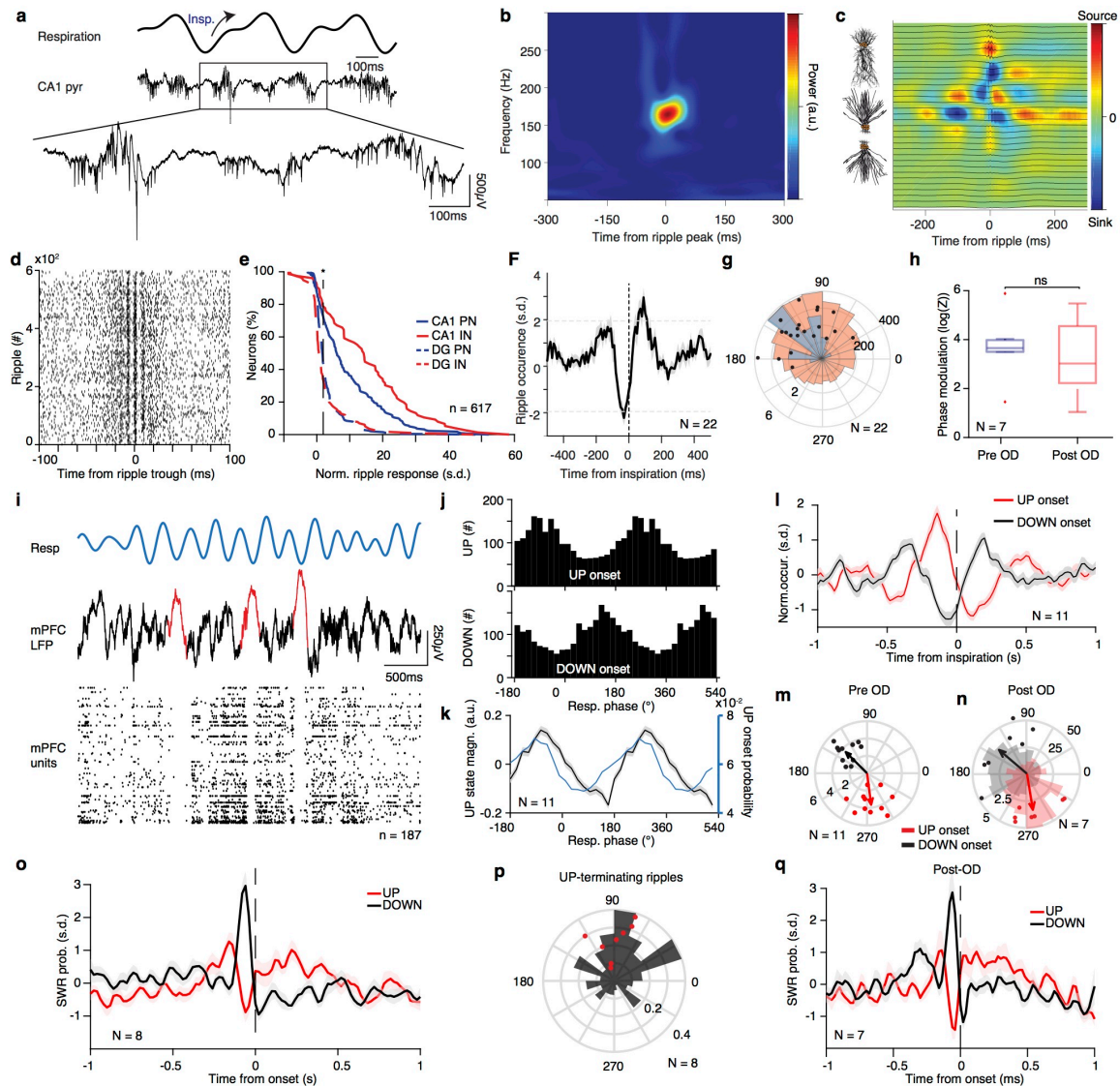


Fig. 6 Breathing modulates hippocampal ripples and cortical UP states.

(a) Example traces of the respiratory signal and CA1 pyramidal layer LFP. In the magnified LFP signal, ripple events and the associated spiking activity can be observed. (b) Average ripple-triggered time-frequency wavelet spectrogram of the CA1 pyramidal layer LFP from one example animal. (c) Schematic of the CA1 pyramidal and granular cells somatodendritic domains aligned to the average ripple-triggered CSD profile of the hippocampal LFP activity for one example animal (See also Supplementary Fig. 8). (d) Ripple-triggered spike train of an example dCA1 neuron exhibiting evoked response and a characteristic oscillatory firing pattern. (e) Cumulative distribution of the ripple-triggered normalized firing of CA1 and DG PNs (CA1, $n = 220$ cells; DG, $n = 202$ cells) and INs (CA1, $n = 76$ cells; DG, $n = 119$ cells). (f) Average cross-correlation between inspiratory events and ripple occurrence ($N = 22$ freely-behaving and head-fixed mice). Dashed horizontal lines indicate the significance levels. (g) Distribution of the respiratory phase of occurrence of individual ripple events for one example animal (red; $n = 4813$ ripples) and preferred phase distribution for the population (blue; $N = 22$ mice). Overlaid, distribution of average phase and modulation strength for ripples (black dots). (h) Phase modulation of ripples before and after OD. (i) Example traces of respiration signal (top), mPFC LFP (middle trace), and spike trains of 187 simultaneously recorded mPFC units during sleep. Three typical delta waves and the corresponding DOWN states of the neuronal population are marked with red. (j) Example distributions of the breathing phase of UP (top) and DOWN (bottom) state onsets. (k) Normalized power (black) and occurrence probability (blue) for prefrontal UP states ($N = 11$ freely-behaving and head-fixed mice). (l) Cross-correlation of UP and DOWN state onsets with respect to inspiration. (m, n) Distribution of preferred breathing phase and phase modulation magnitude ($\log(Z)$) of UP and DOWN states before (m) and after (n) OD. (pre: $N = 11$ mice, post: $N = 7$ mice). Histogram in (n) is for one example session (scale is count of UP/DOWN states). (o) Probability of SWR occurrence as a function of time from UP or DOWN state onset ($N = 8$ mice). (p) Example (black) and distribution of preferred breathing phase of SWR occurrence, for SWRs that are terminating an UP state

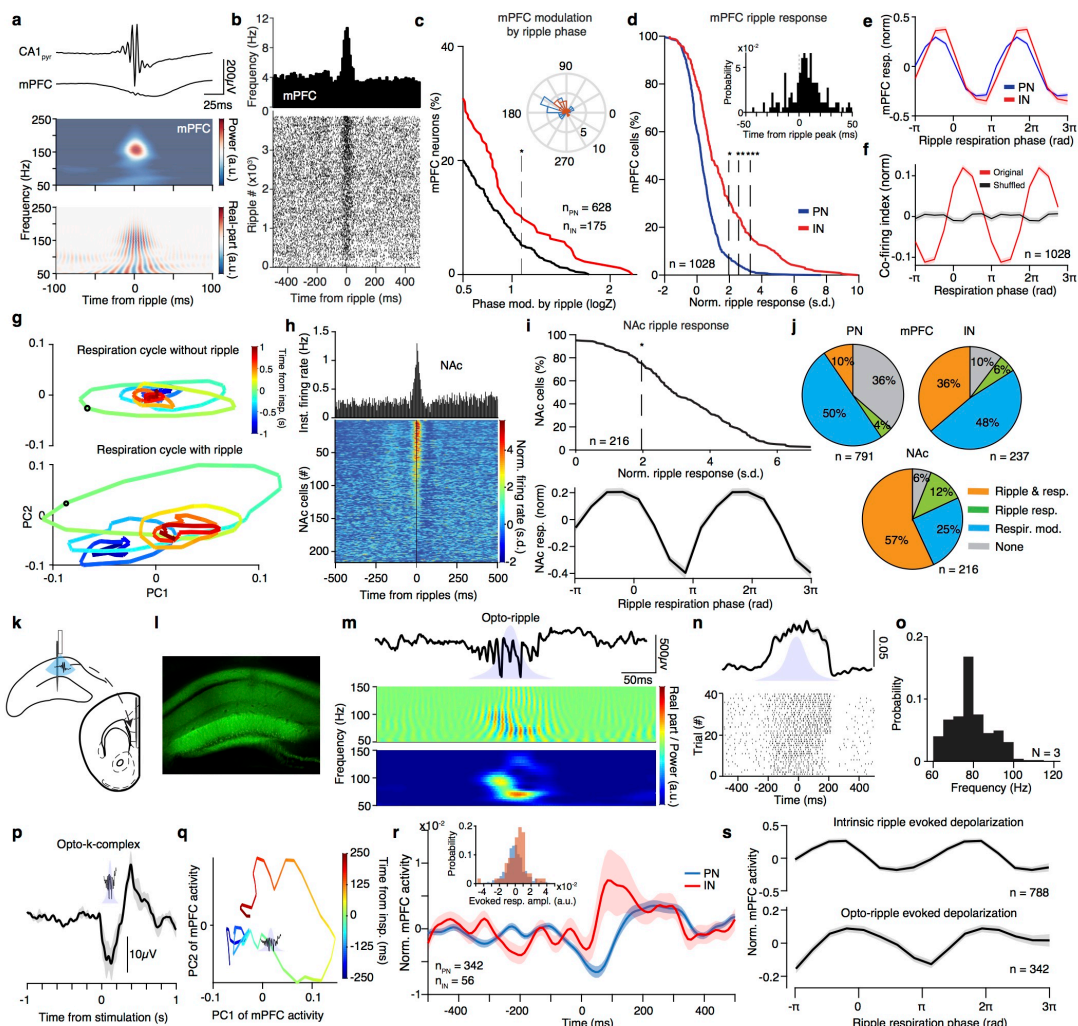
(red dots, $N = 8$ mice). **(q)** Probability of SWR occurrence as a function of time from UP or DOWN state onset after OD ($N = 7$ mice). Note that the observed pattern is identical to pre-OD shown in **(o)**. s.d., standard deviations; a.u., arbitrary units; n.s., not significant; OD, olfactory deafferentation. Shaded areas, mean \pm SEM. Stars indicate significance levels (* $P < 0.05$; ** $P < 0.01$; *** $P < 0.001$).

294 Previous observations during sleep in rats identified a temporal correlation between ripple occurrence and cortical
295 DOWN/UP state complexes^{98,110,112}, with large fraction of ripples preceding DOWN state transition, however the
296 mechanism underlying this correlation remains unknown. We found that ripples preceded the termination of prefrontal
297 UP states and onset of the DOWN states both before (**Fig. 6o**) and after deafferentation (**Fig. 6q**), with ripples
298 associated with UP state termination and immediately preceding a DOWN state onset tended to occur in the early
299 post-inspiratory phase (**Fig. 6p**). This is in line with the RCD-driven synaptic inputs to the DG middle molecular
300 layer preceding ripple events, which are suggesting an RCD-mediated coordination of both cortical and hippocampal
301 excitability favoring SWR co-occurrence with the cortical UP states (**Supplementary Fig. 8c,d**).

302 Ripple output is known to recruit prefrontal neural activity^{98,110}. In agreement with this, hippocampal ripples evoked
303 a response in prefrontal LFP and gave rise to an efferent copy detected as a local increase in fast oscillatory power in
304 the PFC LFP (**Fig. 7a**)⁵⁹. In response to ripple events, $\sim 14\%$ of prefrontal PNs and $\sim 42\%$ of INs exhibited increased
305 firing (**Fig. 7b,d,e** **Supplementary Fig. 8i,l**), while a small fraction of these cells was also rhythmically modulated
306 by the ripple phase (**Fig. 7c**). In parallel, $\sim 69\%$ of NAc cells were significantly driven by ripple events (**Fig. 7h,i**;
307 **Supplementary Fig. 8l**), while in both mPFC and NAc there was a great overlap between cells that were phase
308 modulated by breathing and those that were responsive to ripples (**Fig. 7j**; **Supplementary Fig. 8l**). Importantly, the
309 phase of breathing modulated the excitability of both mPFC and NAc, as revealed by the modulation of ripple-evoked
310 activity magnitude by the phase of breathing (**Fig. 7e,i**), as well as the fine-timescale (10ms) co-firing between CA1 and
311 mPFC (**Fig. 7f**) and within prefrontal regions (**Supplementary Fig. 8e**).

312 Given the observation that prefrontal population activity is limited by the respiratory modulation on a low-dimensional
313 manifold (**Fig. 2d**), we investigated the effect of ripples occurring during inspiration on the trajectory of the neural
314 population activity. Ripples transiently perturbed cortical dynamics, which quickly returned to the respiration-driven
315 limit cycle (**Fig. 7g**).

316 Given the mutual connectivity between the cortical networks and the hippocampus, delineating the causal role of the
317 joint respiratory modulation for the coordination of SWR and UP/DOWN dynamics only by passive observation of the
318 tripartite correlation of cortical, hippocampal and respiratory dynamics is difficult. We thus opted for optogenetically
319 generating ripple oscillations, an experimental manipulation that enabled us to decorrelate the timing of hippocampal
320 ripples from the breathing cycle and thus allowed us to investigate the effect of respiratory modulation of excitability
321 of prefrontal circuits and its sensitivity to SWR-driven inputs. To achieve that, we expressed excitatory opsins in the
322 dCA1 (**Fig. 7l**) and delivered low-intensity half-sine wave light stimulation (**Fig. 7k,m**). Light stimulation resulted in
323 the rhythmic depolarization of dCA1 neurons (**Fig. 7n**) and the generation of short-duration, high-frequency oscillations
324 (termed opto-ripples) (**Fig. 7m**; **Supplementary Fig. 8f**)^{37,115} with peak frequency 75Hz (**Fig. 7o**). These oscillations



332
 333 **Fig. 7 Breathing modulates the cortico-hippocampal interaction.**
 334 (a) Example average ripple-triggered *CA1_{pyr}* and mPFC LFP traces and wavelet spectral decomposition of mPFC LFP power
 335 (upper) and real-part (lower) ($n = 3162$ ripples). (b) Example mPFC unit spiking raster across individual ripples (bottom) and
 336 cross-correlogram of unit firing to ripple (top). (c) Cumulative distribution of the modulation strength by the phase of the hip-
 337 pocampal CA1 ripple oscillation for all mPFC PNs ($n = 628$ cells) and INs ($n = 175$ cells). Inset, distribution of the preferred phase
 338 for all significantly phase-modulated cells. (d) Cumulative distribution of the ripple-triggered normalized firing of mPFC PNs ($n =$
 339 791 cells) and INs ($n = 237$ cells) in response to ripples ($N = 11$ freely-behaving and head-fixed mice). Inset, distribution of time
 340 of unit firing peak from time of ripple peak. (e) Prefrontal ripple-evoked response for PN (blue traces) and IN (red traces), as a
 341 function of the breathing phase of occurrence of ripple. (f) Average normalized co-firing index for all pairs of dCA1 and mPFC cells
 342 ($n = 14412$, $N = 13$ mice) compared to shuffle control. (g) Example trajectory of the mPFC population rate dynamics around the
 343 time of inspiration without (top) and with (bottom) a ripple oscillation occurring during that period in the oscillation. Black circle
 344 denotes time 0, pseudocolor codes for time from inspiration onset. (h) Cross-correlation of firing with respect to ripple time for one
 345 example NAc unit (top) and color-coded cross-correlograms for all NAc cells ($n = 216$ cells). (i) Top, cumulative distribution of the
 346 ripple-triggered normalized firing of NAc cells ($n = 216$ cells) in response to ripples ($N = 4$ mice). Bottom, ripple-evoked response
 347 as a function of the breathing phase of occurrence of ripple. (j) Top, pie charts indicating the percentage of all mPFC PNs (left; n
 348 $= 791$ cells) and INs (right; $n = 237$ cells) that are either phase modulated by respiration (resp. mod), responding significantly to
 349 ripples (ripple resp.), being both significantly modulated by breathing and significantly responsive to ripples or neither. Bottom,
 350 similarly, for all NAc cells ($n = 216$ cells). (k) Schematic of the experimental design for testing the effect of optogenetically induced
 351 hippocampal ripples on the prefrontal network. (l) Example histological reconstruction of the opsin expression in the dorsal hip-
 352 pocampus. (m) Example trace (top) and wavelet real part (middle) and power (bottom) of the oscillation generated in the dCA1
 353 pyramidal layer during the optogenetic stimulation. Note the similarity with ripple oscillations. (n) Cross-correlation of firing with
 354 respect to optogenetic stimulation for one example dCA1 neuron and raster-plot for all events. (o) Probability distribution of the
 355 frequency of evoked oscillations during light stimulation. (p) Example average evoked response in the mPFC LFP triggered on

356 the opto-ripple generation in the dCA1. (q) Example trajectory of the mPFC population around the time of inspiration when an
357 opto-ripple is generated during inspiration. (r) Evoked response in the mPFC neuronal population triggered on the opto-ripple
358 generation in the dCA1. Inset, distribution of the evoked response amplitude for all cells. (s) Normalized prefrontal neuron evoked
359 activity to intrinsic (top) and optogenetically-generated (bottom) ripples, as a function of the respiratory phase of occurrence of
360 the ripple. Shaded areas, mean \pm SEM, s.d., standard deviations; a.u., arbitrary units; FR, firing rate. Stars indicate significance
levels (* $P < 0.05$; ** $P < 0.01$; *** $P < 0.001$).

325 induced evoked activity in the mPFC qualitatively similar to the one described during intrinsic ripples, both at the LFP
326 level, that was consistent with opto-ripple evoked K-complex (**Fig. 7p; Supplementary Fig. 8g**), unit level (**Fig.**
327 **7r; Supplementary Fig. 8h**), and population dynamics (**Fig. 7q**). Interestingly, the magnitude of the prefrontal
328 depolarization in response to opto-ripples was modulated by the ongoing phase of the breathing cycle when opto-
329 ripple was generated, similar to intrinsic ripples (**Fig. 7d, Supplementary Fig. 8i**). A qualitatively similar, though
330 with distinct breathing phase sensitivity, result can be observed in the visually-evoked responses of the visual cortex
331 (**Supplementary Fig. 8j-k**), which constitutes a distinct, LGN-mediated, way of externally probing ongoing cortical
332 dynamics excitability.

362 These results suggest that breathing rhythmically modulates cortical and hippocampal excitability and biases network
363 dynamics in these circuits, as well as their interactions. The joint modulation of these dynamics results in the coordination
364 of emitter and receiver circuits and might contribute to the mechanisms of control of information-flow that enables the
365 integration and segregation of information flow and processing across the network.

Discussion

366 The propagation of information across distinct neuronal networks is facilitated by the coordination of these dynamics
 367 between brain regions^{7,112}. In this study, we demonstrate that the respiratory rhythm, via a centrifugal corollary dis-
 368 charge, acts as a functional oscillatory scaffold and provides a unifying global temporal coordination of neuronal firing
 369 and network dynamics across cortical and subcortical networks during offline states. The comprehensive phase-resolved
 370 picture of this synchronization provides the basis for mechanistic theories of information-flow across the limbic system
 371 (**Fig. 8b**).

Respiratory corollary discharge couples global brain circuits

372 Using pharmacological manipulations paired with large-scale recordings, we identified a joint mechanism of respiratory
 373 entrainment, consisting of an efference copy of the brainstem respiratory rhythm or vagal re-afferents (respiratory corollary
 374 discharge; RCD) that underlies the neuronal modulation of brain regions and a respiratory olfactory refference (ROR)

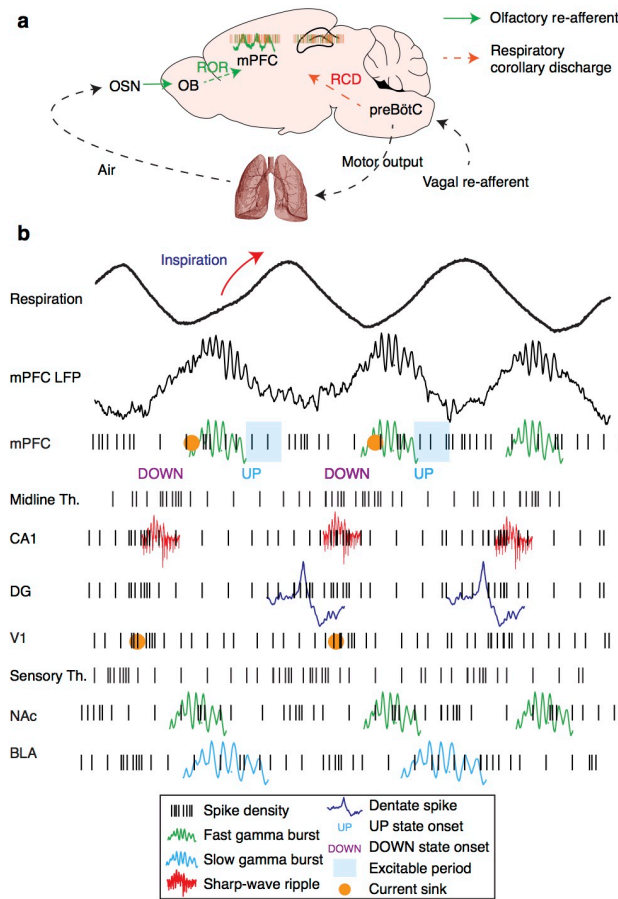


Fig. 8 Breathing organizes network dynamics across limbic structures.
 (a) Schematic depiction of the efferent copy pathway carrying the respiratory corollary discharge (RCD) signal and the refferent pathway carrying the respiratory olfactory refferent (ROR) signal. (b) Summary schematic of the network dynamics organized by breathing throughout all structures studied. Black traces: LFPs; Black ticks: neuronal spikes; Green traces: Fast (~80Hz) gamma; Cyan traces: Slow gamma (~40Hz); Red traces: CA1 Ripples; Blue traces: Dentate spikes; Orange dots: CSD sinks (mPFC deep layers, V1 LGN input, and DG middle molecular layer); Blue shadow: Cortical excitability period.

375 that contributes to the modulation and accounts for respiration-locked LFP signals (**Fig. 8a**). We have demonstrated
376 the global entrainment of neuronal activity by the respiratory rhythm that is mediated by the intracerebral RCD, likely
377 originating in the brainstem rhythm generator circuits and being unaffected by olfactory deafferentation.

378 Brainstem circuits are well-known to generate breathing rhythm independently of descending forebrain inputs and at
379 the same time send massive diffuse ascending projections to the forebrain, thus the most parsimonious explanation of
380 the observed phenomenon is a directional drive from the brainstem to the forebrain. While descending feedback inputs
381 might modulate breathing and contribute to the phenomenon, they are not serving the rhythm generation function,
382 which is known to be implemented in the brainstem circuits that provide a causal effect on the forebrain circuits. OD
383 experiments result in a virtually absent spectral peak in the prefrontal LFP and reduction of gamma and unit entrainment
384 across different circuits, while respiratory activity is unchanged. This strongly suggests the same directionality of the
385 phenomenon as suggested by the analytical methods.

386 These results highlight the global extent and significance of this modulation, given the crucial role that the interaction
387 between limbic structures plays for emotional processing and memory functions. Although the pathways mediating RCD
388 remain unknown, we speculate that ascending long-range somatostatin-expressing cells, projecting from the preBötzing
389 complex to the thalamus, hypothalamus, and basal forebrain¹³² or the locus coeruleus¹³⁰, are probable pathways for
390 this widespread modulation. An alternative source of such modulation could be ascending vagal re-afferents^{24,89}. A
391 disinhibition-mediated mechanism of RCD would be consistent with the lack of prominent LFP sources in the absence of
392 ROR following olfactory deafferentation, similar to the mechanism of disinhibitory pacing by the medial septum of the
393 entorhinal-hippocampal system during theta oscillations¹⁵. The global and powerful nature of the RCD suggests that
394 potentially multiple parallel ascending pathways from the brainstem mediate this signal redundantly and calls for future
395 tracing and activity-dependent labeling studies to identify its anatomical substrate.

396 We suggest that centrifugal modulation by breathing is analogous to the predictive signaling employed in a wide range
397 of neural circuits²⁸, such as those underlying sensory-motor coordination¹¹⁷ and likely extends to other brain structures
398 and brain states. The global outreach of RCD to higher-order areas suggests that it might play an important role in the
399 coordination of multi-sensory processing, in sync with orofacial motor output during both passive and active orofacial
400 sampling, thus providing a centrifugal component synchronized with refferent sensory inputs and respiratory efference
401 copies to orofacial motor centers⁸⁴.

402 Extending the generality of respiratory rhythm entrainment, we show that fear-related 4 Hz oscillations^{31,57} are
403 a state-specific expression of this entrainment and originate from the refferent respiratory entrainment of olfactory
404 sensory neurons by passive airflow⁴⁶. Importantly, although prefrontal 4 Hz LFP oscillations originate in fear-associated
405 enhanced breathing, the ROR is not necessary for the expression of innate or conditioned fear behavior, in agreement with
406 a recent report⁸³. This suggests the potential sufficiency of RCD for the expression of fear behavior. Consistent with such
407 mechanism, the optogenetic induction of 4 Hz oscillations in prefrontal circuits is sufficient to drive fear behavior in naïve
408 animals⁵⁷, raising the possibility that this effect is mediated by the bidirectional interaction of prefrontal networks with
409 the respiratory centers via top-down projections to periaqueductal gray and the ascending feedback via RCD giving rise

410 to system-level resonance at breathing frequency. This sets the stage for future investigations of the interaction between
411 the RCD and ROR in limbic networks and, in turn, the top-down modulation of breathing and emotional responses.

Breathing rhythm contributes to synchronization of the cortico-hippocampal dynamics - Implications for models of memory consolidation

412 Mechanistic theories of systems memory consolidation posit that synchronous network activity plays a central role in
413 attractor dynamics underlying the reactivation of memory traces and coordination of information flow. The original
414 two-stage model proposed a central role of hippocampal SWR in broadcasting memory traces¹⁴, while the fine-timescale
415 relationship of SWR and neocortical DOWN/UP state dynamics^{51,111} led to an update of the model that posited active
416 functional role of slow oscillations in bringing cortico-hippocampal dynamics together and thus providing coordinated
417 windows of opportunity for information flow^{7,112}. While a critical role of SWR and their coordination with DOWN/UP
418 states for memory consolidation has been demonstrated^{44,73}, there is no established mechanism mediating the coordi-
419 nation of SWR with distributed neocortical DOWN/UP state dynamics and, importantly, other brain structures that
420 take part in memory consolidation. Here we demonstrated that the respiratory rhythm coordinates cortico-hippocampal
421 dynamics as well as unit activity across the limbic system, with RCD being a sufficient mechanism. Furthermore, we
422 show that respiratory coordination modulates the responsiveness of downstream prefrontal and nucleus accumbens popu-
423 lations to hippocampal SWR and CA1-mPFC unit cofiring, suggesting that respiratory phase biases interaction between
424 these circuits. This respiration-coordinated circuit interaction model extends previously observed bivariate correlations
425 between SWR and prefrontal^{55,110}, accumbens⁹⁴, and amygdala⁴³ neural activity, as well as respiratory entrainment of
426 hippocampal units^{68,87,133} and ripples⁶⁷, which can, in part, be accounted for by the respiratory comodulation demon-
427 strated here. This does not imply the necessity of respiratory modulation for reactivation *per se*, or that reactivation in
428 limbic structures occurs specifically in temporal association with SWR, but that temporal correlation between population
429 activity in all the respected structures, in addition to direct connectivity, is comodulated by a common rhythm that can
430 support effective information transfer.

431 Based on CSD analysis and pharmacological manipulation, we suggest that RCD and ROR inputs, via MEC and
432 LEC respectively, give rise to hippocampal unit modulation, RCD likely responsible for the emergence of dentate spikes
433 and SWR respiratory-entrainment. Depending on its strength, the RCD input, either via feed-forward inhibition of
434 the CA3¹ or forward excitation can, respectively, delay or advance SWRs within the respiratory cycle. In parallel, the
435 ripple-driven recruitment of prefrontal neurons likely triggers the resetting of the ongoing UP states by tilting the bias
436 between excitation and inhibition¹⁰⁸ and results in a feedback re-entrance to the entorhinal-hippocampal network⁵¹. In
437 concert with this bidirectional interaction, the intrinsic RCD-mediated co-modulation of SWR and DOWN/UP state
438 complexes by the breathing phase is likely setting up the functional sequences of these nonlinear dynamics that are critical
439 for memory consolidation. Indeed, breathing rhythm biases the occurrence of SWR prior to DOWN state onset (**Fig.**
440 **6o**)^{99,111}, while the causal enhancement of this pattern improves memory consolidation⁷³. Understanding the causal
441 role of respiratory entrainment in the synchronization of cortico-hippocampal dynamics will require dissection of circuit

442 mechanisms of RCD and fine-timescale, closed-loop optogenetic perturbations. Our causal optogenetic manipulation of
443 one side of this complex dynamical system identifies an excitability profile of hippocampo-cortical interaction within a
444 breathing cycle and paves the way for future respiration phase-resolved gain of function studies.

445 While we show here that the respiratory dynamics bias the prefrontal DOWN/UP states via RCD, slow oscillations
446 can emerge in isolated cortical slubs¹²¹ or slices¹⁰⁵ and thus slow oscillations observed at a similar frequency in the tha-
447 lamocortical system across all mammalian species¹⁸ are not necessarily forced by the breathing rhythm^{68,126}. Rather,
448 we suggest considering their interaction from the mechanistic dynamical systems perspective of coupled bistable non-
449 linear dynamical systems. Indeed, leading models of the generation of neocortical UP states from DOWN states²⁵ or
450 inspiratory bursts from expiratory silence in preBötzinger circuits³² suggest that both phenomena rely on regenerative
451 avalanches, due to recurrent connectivity, that are followed by activity-dependent disfacilitation. Given that neocortical
452 slow oscillations can be locally generated^{112,128}, are globally synchronized by the thalamic input⁶⁵ and propagate across
453 the neocortex^{51,76}, RCD biasing of the cortical DOWN/UP state complex could be considered as an extension of a global
454 system of mutually-coupled nonlinear oscillators. The persistent synchronous output of the respiratory oscillator and its
455 marginal independence of the descending input might provide a widespread asymmetric bias to both cortical DOWN/UP
456 states and hippocampal SWR across offline states of different depth. It is likely, however, that via descending cortical
457 projections, cortical SO provides feedback to the pontine respiratory rhythm-generating centers and thus the interaction
458 between respiratory dynamics and slow oscillations could be bidirectional. Further, transient cessation of breathing dur-
459 ing apnea or extended expiration could provide windows of low impact of breathing rhythm on the dynamics, whereas
460 frequency fluctuations of the respiratory rhythm compress or stretch the ongoing cortical dynamics (**Supplementary**
461 **Fig. 3g**). The functional implications of these phenomena for the coordination of network dynamics remain to be studied.
462 Nevertheless, the interactions of cortico-hippocampal dynamics and bivariate interactions between different structures
463 based on their direct connections might be sufficient for providing a high degree of correlation that doesn't decorrelate
464 over short periods devoid of breathing pacing.

465 Finally, the perpetual comodulation of limbic population activity by breathing also suggests a potential framework
466 for memory consolidation processes that do not rely on deep sleep and the associated synchronous cortical DOWN/UP
467 states, that could explain the mechanism and distinctive role of awake replay in memory consolidation^{23,37,54}.

Olfactory bulb reafferent source of LFP signals and gamma oscillations

468 Respiratory olfactory reafferent input, in the form of synchronous recruitment of olfactory bulb by sensory input, organizes
469 internal dynamics in OB circuit^{42,72,100} and gives rise to entrainment and macroscopically observed respiration-coherent
470 LFP signals in the downstream structures^{9,39,53,58,83,136}. Our results extend and provide a mechanistic explanation
471 and interpretation of the emergence of respiration-related LFP signals in these regions, dissociating them from the
472 centrifugal RCD-mediated mechanism of entrainment of the neural activity. We further report the reafferent OB origin
473 of local gamma dynamics and their modulation by breathing, as well as the relation between local gamma oscillations

474 and neuronal activity in all structures. This sheds new light onto the origin and role of prefrontal^{113,136}, BLA^{27,118}, and
475 NAc²² gamma oscillations and calls for scrutiny in LFP gamma analyses.

476 Anatomically-resolved analysis of prefrontal OB-generated current sources and unit activity suggests that deep layers
477 and mostly ventral regions are the main targets of OB refference and give rise to observed LFP signals. Although the
478 interpretation of these gradients is challenging given the existence of volume conduction from the OB, these findings
479 suggest a potential functional role of the differential modulation of orbital, prefrontal, and cingulate regions and is worthy
480 of future investigation. Importantly, the propagation of respiration-driven excitation to distant structures is jointly driven
481 by both ROR and RCD, the former giving rise to observed LFP signals that disappear after OD, as shown here, or OB
482 ablation^{9,53,83}. Thus, due to the fast breathing frequency in mice, slow and/or delta power cortical LFP signals are in
483 part, and depending on the synaptic distance from the OB, contaminated by ROR, making the direct analysis of slow
484 oscillation or delta waves based on LFP signal alone unreliable. Further investigations are required to dissociate the
485 differential functional role of ROR and RCD in recruiting brain circuits to the breathing rhythm.

486 This joint modulation of downstream circuits suggests a model in which synchronous ROR inputs reach the target
487 regions in sync with RCD-coordinated local activity. These oscillations potentially provide a temporally-optimized privi-
488 leged route for olfactory refferent input to affect the ongoing cortical activity, in line with recent reports in humans¹³⁵.
489 This could explain the efficacy of experimental manipulations that bias learning⁴, consolidation¹⁰², or sleep depth⁹⁶
490 using odor presentation during sleep which suggest that olfaction is a royal path to the sleeping brain.

Outlook

491 Finally, in light of the wide modulation of multiple circuits by breathing during quiescence, we suggest that breathing
492 effectively modulates the default mode network (DMN). To examine this hypothesis future work will be needed to
493 carefully examine the fine temporal structure of neuronal assemblies and their modulation by the RCD and ROR copies
494 of the breathing rhythm throughout cortical and subcortical structures, an endeavor that might uncover functional sub-
495 networks of the DMN. The mechanisms responsible for the widespread pacing of limbic circuits by breathing identified
496 here might underlie the powerful role of breathing in spiritual and rehabilitation practices¹² and emotional disturbances
497 in patients^{45,62,86}.

498 In summary, the data provided here suggest that breathing provides a constant stream of rhythmic input to the brain.
499 In addition to its role as the *condicio sine qua non* for life, we provide evidence that the breathing rhythm acts as a global
500 pacemaker of the brain, providing a persistent corollary discharge signal that enables the integration and segregation
501 of information flow and processing across the distributed circuits by synchronizing local, internally-generated dynamics
502 during offline states. In this emergent model of respiratory entrainment of limbic circuits, we speculate that this perennial
503 rhythm not only coordinates memory consolidation dynamics during offline states but likely enables the integration of
504 exteroceptive and interoceptive inputs and internal representations into coherent cognitive manifolds across multiple
505 mental states.

Acknowledgments

506 We thank E. Blanco Hernandez for input and help with histological verification of olfactory deafferentation, G. Schwesig,
507 and E. Resnik for valuable input, R. Ahmed for technical assistance, J. Lu for assistance in the experiments, S. Masmanidis
508 for providing silicon probes, and all the members of the Sirota laboratory for helpful discussions and comments on the
509 manuscript. This work was supported by grants from Munich Cluster for Systems Neurology (SyNergy, EXC 1010),
510 Deutsche Forschungsgemeinschaft Priority Program 1665 and 1392 and Bundesministerium für Bildung und Forschung
511 via grant no. 01GQ0440 (Bernstein Centre for Computational Neuroscience Munich), European Union Horizon 2020
512 FETPOACT program via grant agreement no.723032 (BrainCom) (A.S.), and EMBO Long-Term Fellowship (N.K.).

Author Contributions

513 N.K and A.S. designed the experiments and data analysis, interpreted the data and wrote the manuscript, N.K. performed
514 the experiments and analyzed the data.

Competing Interests

515 The authors declare no competing interests.

Methods

Animals

516 Naive male C57BL6/J mice (3 months old, Jackson Laboratory) were individually housed for at least a week before
517 all experiments, under a 12 light-dark cycle, ambient temperature 22 °C and provided with food and water *ad libitum*.
518 Experiments were performed during the light phase. All procedures were performed in accordance with standard ethical
519 guidelines and in accordance with the European Communities Directive 2010/63/EC and the German Law for Protection
520 of Animals (Tierschutzgesetz) and were approved by local authorities (ROB-55.2-2532.Vet_02-16-170). All efforts were
521 made to minimize the number of animals used and the incurred discomfort.

Surgery

522 Anesthesia was induced with a combination of medetomidine (0.5 mg/kg), midazolam (5 mg/kg), and fentanyl (0.05
523 mg/kg) and surgical plane of anesthesia was maintained using 1% Isoflurane in O_2 . Body temperature was maintained
524 at 37 °C with a custom heating pad. Analgesia was provided by means of subcutaneous administration of metamizol
525 (200 mg/kg) and local subcutaneous administration of a mixture of lidocaine (5 mg/kg) and bupivacaine (5 mg/kg)
526 during OP and meloxicam (1 mg/kg) for 7 days post-operatively. Enrofloxacin (5 mg/kg, subcutaneous administration)
527 was also provided post-operatively. For free behavior recordings, electrode bundles, multi-wire electrode arrays, or silicon
528 probes were implanted chronically. Recordings targeted the medial prefrontal cortex (stereotaxic coordinates: 1.7-2 mm
529 anterior to the bregma (AP), 0.3 mm lateral to the midline (ML) and 0.8 to 1.4 mm ventral to the cortical surface
530 (DV)), dorsal hippocampus (AP: -2.3 mm, ML: 1.5 mm, DV: 0.8-1.5 mm), V1 (AP: -3.0 mm, ML: 2.3 mm), BLA
531 (AP: -1.7 mm, ML: 3 mm, 4 mm DV) and NAc (AP: 1.2 mm, ML: 1 mm, DV: 4 mm)⁹³. For head-fixed recordings, a
532 craniotomy above the targeted structure and a midline bilateral craniotomy above the mPFC was performed to enable
533 the recording from all cortical layers. Dura was left intact and craniotomies were sealed with Kwik-Cast (WPI, Germany)
534 after surgery and after each recording session. For electromyographic (EMG) and electrocardiographic (ECG) recordings,
535 two 125 μ m Teflon-coated silver electrodes (AG-5T, Science Products GmbH) were sutured into the right and left nuchal
536 or dorsal intercostal muscles, using bio-absorbable sutures (Surgicryl Monofilament USP 5/0). Wires were connected to
537 a multi-wire electrode array connector (Omnetics) attached to the skull. For the recording of the neural activity of the
538 olfactory epithelium, which was used as a proxy for respiration⁹¹, a small hole was drilled above the anterior portion
539 of the nasal bone (AP: +3 mm from the nasal fissure, ML: +0.5 mm from midline) until the olfactory epithelium was
540 revealed. A 75 μ m Teflon-coated silver electrode (AG-3T, Science Products GmbH) was inserted inside the soft epithelial
541 tissue. Approximately 500 μ m of insulation was removed from the tip of this wire and the other end was connected
542 to the same Omnetics connector as the rest of the electrodes. Two miniature stainless steel screws (#000-120, Antrin
543 Miniature Specialties, Inc.), pre-soldered to copper wire were implanted bilaterally above the cerebellum and served as
544 the ground for electrophysiological recordings and as an anchoring point for the implants. All implants were secured

545 using self-etching, light-curing dental adhesive (OptiBond All-In-One, Kerr), light-curing dental cement (Tetric Evoflow,
546 Ivoclar Vivadent) and autopolymerizing prosthetic resin (Paladur, Heraeus Kulzer).

Behavior

547 Electrophysiological recordings of the mice took place before and after each behavioral session in the home-cage. Home-
548 cage consisted of clear acrylic filled with wood chip bedding and a metal grid ceiling which was removed for the purposes
549 of the recordings. Food pellets were distributed in the home-cage and water was placed inside a plastic cup. Nesting
550 material was available in the home-cage and utilized by the mice (typically building a nest in a corner). Exploratory
551 behavior was recorded in a cheeseboard maze, consisting of a 60cm diameter acrylic cylinder with wooden laminated
552 floor perforated with 10 mm diameter holes. For recordings of mice running freely on a wheel, a horizontal wheel (Flying
553 Saucer) was permanently placed inside the homecage. The mice typically exhibited long running episodes on the wheel,
554 with interspersed sleep episodes. Fear conditioning took place in context A, which consists of a square acrylic box (30
555 cm x 30 cm x 30 cm). Walls were externally decorated with black and white stripes. The box was dimly lit with white
556 LEDs (25 lux) and white noise background sound was delivered through the walls using a surface transducer (WHD
557 SoundWaver). The floor consisted of a custom-designed metal grid (6 mm diameter stainless steel rods) connected to
558 a precise current source (STG4004-1.6mA, Multi Channel Systems MCS GmbH). On day 1, mice were subjected to a
559 habituation session in context A, during which the CS^+ and CS^- (7.5 kHz, 80 dB or white-noise, 80 dB) were presented
560 4 times each. Each CS presentation consisted of 27 pips (50 ms duration, 2 ms rise and fall) with 1.1 s inter-pip interval.
561 On the same day, in the fear conditioning session, CS^+ was paired with the US. To serve as US, a mild electric foot-shock
562 (1 s duration, 0.6 mA, 50 Hz AC, 5 CS-US pairings, 20-60 s randomized inter-trial intervals) was delivered to the mice
563 through the metal grid. The onset of the foot-shock coincided with the offset of the conditioned stimulus. During the
564 memory retrieval session, mice were presented with 4 CS^- and 4 CS^+ presentations 24 hours after conditioning, in a
565 distinct context B. For experiments involving pharmacological manipulation, a second retrieval session took place 12
566 days after fear conditioning. For experiments involving innate fear responses, mice were exposed for 10 min to a neutral
567 context while a small filter paper, scented with the odorant 2-methyl-2-thiazoline (2MT) (M83406-25G; Sigma Aldrich),
568 was placed in the environment. 2MT is a synthetic odorant, chemically related to the fox anogenital gland secretion
569 2,4,5-trimethyl-3-thiazoline (TMT), that induces robust innate fear responses, in contrast to TMT⁵². The sequence of
570 the experimental protocol is schematized in **Supplementary Fig. 2a**.

Behavioral analysis and state segmentation

571 An important parameter for the behavior related analysis of neuronal activity is the proper determination of the behav-
572 ioral state of the animal. For the purpose of behavioral state detection in freely-behaving mice, the movement of the
573 animal was tracked using a 3-axis accelerometer (ADXL335, Analog Devices) incorporated in the headstage, which was
574 used as the ground truth for the head-motion. Accelerometer data were sampled at 30 kHz and the sensitivity of the
575 accelerometer is 340 mV/g (g is the standard acceleration due to gravity; $\sim 9.8m/s^2$). The gravity vector is differentially

576 reflected in the different axes as a function of posture. Since the accelerometer measures simultaneously the dynamic
577 acceleration due to head movement and the static acceleration due to gravity, the first time derivative of the acceleration
578 was calculated (jerk; units: g/s). This measure eliminates the effect of gravity and the dynamic acceleration dominates.
579 The effect of gravity on the different axes is amplified during head rotations. The jerk of each axis was analyzed separately
580 for the quantification of head-motion, however for the behavioral state detection the magnitude of the jerk was quantified
581 as: $J = \sum_{k=1}^3 \left| \frac{\partial \vec{a}_k}{\partial t} \right|$, where \vec{a}_k is the acceleration for each axis and smoothed in time using a narrow Gaussian window
582 (2 s, 100 ms s.d.) (**Supplementary Fig. 1e**). This head micro-motion is not used to extract the respiration signal used
583 throughout the manuscript, which is instead recorded from the nasal cavity. The only exception is **Supplementary Fig.**
584 **1a** and **Supplementary Fig. 2c,d**, where the head-mounted accelerometer signal is also used for purely demonstration
585 purposes, to highlight the fact that respiration is also reflected in the head micromotions.

586 Additionally, the activity of mice was tracked using an overhead camera (Logitech C920 HD Pro). The camera data
587 were transferred to a computer dedicated to the behavior tracking and were acquired and processed in real-time using a
588 custom-designed pipeline based on the Bonsai software⁷⁰. Video data were synchronized with the electrophysiological data
589 using network events. Video was preprocessed to extract the frame-to-frame difference and calculate a compound measure
590 that we found provided an excellent proxy for the behavioral state. Video frames were thresholded and binarized. A logical
591 exclusive OR operation was applied on consecutive frames, a calculation that provides the effective frame difference. The
592 sum of these differences provides a measure of overall change between consecutive frames. We found that the changes
593 in the amplitude of variance of this measure over time are informative for the current state of the mouse. Complete
594 immobility is easily distinguishable using this measure, due to the low amplitude and small variance of the signal. A
595 threshold was set manually such that even small muscle twitches during sleep were captured, but breathing-related
596 head-motion was below threshold. Using the density of head micro-motions and muscle twitches, we were able to classify
597 behavioral segments as active awakening, quiescence, or sleep (**Supplementary Fig. 1f**). For head-fixed recordings, we
598 relied solely on high-resolution video of the mouse snout and body, from which we derived a micro-motion signal that
599 was used in the same way as the jerk-based signal for freely-behaving mice.

Head-fixed recordings

600 For high-density silicon probe recordings, we exploited the advantages of the head-fixed mouse preparation. Large-
601 scale neuronal recordings reported are collected with the following methods in head-fixed mice, unless otherwise noted
602 in the figure legends. Mice were implanted with a lightweight laser-cut stainless steel headplate (Neurotar) above the
603 cerebellum. After recovery from surgery, mice were habituated daily for 3-4 days to head-fixation prior to experimentation.
604 A modified Mobile HomeCage (Neurotar) device was used, enabling mice to locomote, rest, and occasionally transition
605 to sleep, within a customized free-floating carbon fiber enclosure (180 mm diameter and 40 mm wall height). Animal
606 behavior was monitored using two modified 30fps, 1080p infrared cameras (ELP, Ailipu Technology Co), equipped with
607 modified macro zoom lenses.

In vivo electrophysiology

608 LFP and single-unit activity were recorded using either 12.5 μ m Teflon coated Tungsten wire (California Fine Wire)
609 or custom-designed silicon probes (Neuronexus and UCLA)¹³¹. High-density silicon probes (A1x64-Poly2-6mm-23s-160)
610 were used for hippocampal CSD profiles, prefrontal depth profiles while multi-shank probes were used for prefrontal
611 CSD analyses (A16x1-2mm-50-177). Individual electrodes or probe sites were electroplated to an impedance of 100-400
612 k Ω (at 1 kHz) using a 75% polyethylene glycol - 25% gold³⁵ or PEDOT solution⁷¹. NanoZ (White Matter) was used
613 to pass constant electroplating current (0.1 – 0.5 μ A) and perform impedance spectroscopy for each electrode site. A
614 reversed-polarity pulse of 1 s duration preceded the plating procedure to clean the electrode surface. After electroplating,
615 electrodes impedance was tested in saline (at 1 kHz) and arrays were checked for shorts. Electrodes were connected to
616 RHD2000 chip-based amplifier boards (Intan Technologies) with 16-64 channels. Broadband (0.1 Hz-7.5 kHz) signals
617 were acquired at 30 kHz. Signals were digitized at 16 bit and multiplexed at the amplifier boards and were transmitted
618 to the OpenEphys recording controller using thin (1.8 mm diameter) 12-wire digital SPI (serial peripheral interface)
619 cables (Intan Technologies). Typically 32-256 channels were recorded simultaneously. Data acquisition was synchronized
620 across devices using custom-written network synchronization code.

Respiration measurement

621 Breathing was measured using EOG recordings⁹¹, implanted as described in the Surgery section. Following OD, the
622 amplitude of the EOG signal was dramatically reduced. To quantify the effect of this manipulation on the neuronal
623 entrainment by breathing, we additionally recorded the respiratory rhythm using a fast response thermistor (GLS9-MCD,
624 TE Connectivity) placed in close proximity to the naris of head-fixed mice.

Anatomical analysis

625 After plating, electrodes and silicon probes were coated with DiI (ThermoFischer Scientific), a red fluorescent lipophilic
626 dye³³. Upon insertion in the brain, the dye is slowly incorporated in the cell membranes and diffuses laterally along the
627 membrane, allowing the visualization of the electrode track and the histological verification of the electrode position.
628 After the conclusion of the experiments, selected electrode sites were lesioned by passing anodal current through the
629 electrode¹²⁰. Typically, 10 μ A current was passed for 5 s to produce lesions clearly visible under the microscope. One
630 day was allowed before perfusion, to enable the formation of gliosis. Electrode tip locations were reconstructed with
631 standard histological techniques. Mice were euthanized and transcardially perfused through the left ventricle with 4% EM
632 grade paraformaldehyde (PFA) (Electron Microscopy Sciences) in 0.1 M PBS. Brains were sectioned using a vibratome
633 50 – 80 μ m thick sections) and slices were stained with DAPI and mounted on gelatin-coated glass microscopy slides.

LFP analysis

634 Raw data were converted to binary format, low pass-filtered (0.5-400 Hz) to extract the local field potential component
635 (LFP) and downsampled to 1 kHz. LFP signals were filtered for different frequency bands of interest using zero-phase-
636 distortion sixth-order Butterworth filters. All data analysis was performed using custom-written software. Neuroscope
637 data browser was used to aid with data visualization⁴⁷.

Spectral analysis

638 LFP power spectrum and LFP-LFP coherence estimations were performed using multitaper direct spectral estimates.
639 For respiration frequency analyses, data were padded and a moving window of 3 s width and 2.4 s overlap was applied
640 to the data. Signals were multiplied with 2 orthogonal taper functions (discrete prolate spheroidal sequences), Fourier
641 transformed and averaged to obtain the spectral estimate⁷⁹. Magnitude-squared coherence was calculated using these
642 multitaper direct spectral estimates. For gamma frequency analyses, a window of 100 ms with 80 ms overlap, and 4
643 tapers were used. For some analyses and examples, to obtain a higher resolution in both time and frequency domain,
644 data were transformed using complex Morlet wavelets (bandwidth parameter: 3, center frequency: 1.5). Convolution of
645 the real and imaginary components of the transformed signal enables the extraction of the instantaneous amplitude and
646 phase of the signal for each scale. For some example signal visualizations, we found it useful to utilize the real-part
647 of the wavelet transformed signal, which preserves both phase and amplitude information (**Fig. 7a**). For the power
648 comodulation analysis⁷⁵, the instantaneous multitaper estimate of the spectral power time series for each frequency bin
649 in each structure was calculated and the Spearman correlation coefficient of every pair was calculated. To characterize
650 the causal relationship between the respiratory signal and the prefrontal LFP, spectrally resolved Granger causality
651 was calculated using the multivariate Granger causality toolbox⁵. Briefly, unfiltered LFP traces were detrended and
652 normalized. The order of the vector autoregressive (VAR) model to be fitted was calculated using the Akaike information
653 criterion. To correct for the effect of SNR differences on Granger causality estimates, Granger-causality was calculated
654 for both the original and the time-reversed signals and compared¹²⁷ (**Supplementary Fig. 1i**).

655 To establish the phase shift between two different signals, we used two different approaches, one in the time and the
656 other in the phase domain. In the time domain (e.g. Supplementary Fig. 1B left), we detected the troughs or peaks of one
657 signal (using a local minima detection algorithm on the bandpass filtered signal) and used these times to calculate the
658 triggered average of the second signal. For the phase domain analyses (e.g. Supplementary Fig. 1B right), we calculated
659 the instantaneous phase of each of the signals (as the four-quadrant inverse tangent of the analytical signal calculated
660 from the Hilbert transform of the narrow-bandpass-filtered signal) and plotted the distribution of point-to-point phase
661 differences.

Phase modulation analysis

662 For phase analyses, the signal was filtered in the desired narrow frequency band and the complex-valued analytic signal
663 was calculated using the Hilbert transform $\rho(t) = e^{-i\phi(t)}$. The instantaneous amplitude at each timepoint was estimated
664 based on the vector length, while the instantaneous phase of the signal was computed as the four-quadrant inverse
665 tangent of the vector angle. A phase of 0° corresponds to the peak of the oscillation and a phase of 180° to the trough
666 of the oscillation. The waveshape of the respiratory signal and its LFP counterparts are highly asymmetric, resulting in
667 non-uniform phase distribution of this reference signal (**Supplementary Fig. 3c**). This deviation from uniformity is
668 catastrophic for the phase modulation statistics since it biases the phase detection leading to false positive results. To
669 account for this potential bias, the circular ranks of the phase distribution were computed and the phase distribution
670 was transformed using the inverse of the empirical cumulative density function (ECDF) to return a signal with uniform
671 prior distribution. After this correction, the phases can be assumed to be drawn from a uniform distribution enabling
672 the unbiased application of circular statistics^{57,109,113}. Point-processes with <200 events in the periods of interest were
673 excluded from phase analyses, due to sample-size bias of these analyses¹¹³. For the quantification of phase modulation,
674 the variance-stabilized log-transformed Rayleigh's test $Z(\log(\frac{R^2}{n}))$, where R is the resultant length and n the sample size,
675 \log is natural logarithm) was used^{57,109,113}. This statistic quantifies the non-uniformity of a circular distribution against
676 the von Mises distribution. Since ECDF transformation nonlinearly distorts the phase, non-corrected phase samples were
677 used for characterizing the preferred phase.

Phase-amplitude cross-frequency coupling

678 For power-phase cross-frequency coupling, the modulation index (MI), as well as the mean resultant length (MRL), was
679 calculated for each phase and amplitude pair¹²². Phase was evaluated for 1-20 Hz with a bandwidth of 1 Hz and step of
680 0.2 Hz using the Hilbert transform and correction for non-uniformity as described above. The amplitude was evaluated
681 for 20-120 Hz with 5 Hz bandwidth and 3 Hz step. Shuffling statistics were used to evaluate the statistical significance
682 of the MI and MRL by shuffling the phase and amplitude values.

Current-source density analysis

683 Current-source density analysis was performed using the inverse CSD method⁹⁷ with activity diameter 1 mm for slow
684 and 0.5 mm for fast network events, 0.05 s.d., smoothed using varying cubic splines and extracellular conductivity $\sigma =$
685 $0.3S/m$ based on calculations of isotropic and ohmic tissue impedance^{69,101}. Importantly, all results were qualitatively
686 confirmed by exploring the parameter space as well as using the classic second derivative CSD estimation method⁸⁸.
687 Occasional malfunctioning recording sites were interpolated from neighboring sites and all relevant sinks and sources
688 were characterized and quantified from portions of data with no interpolated sites.

Layer assignment

689 For the hippocampal high-density silicon probe recordings, channel layer assignment was performed based on established
690 electrophysiological patterns of activity for different laminae¹⁵. The middle of the pyramidal layer was assigned to the
691 channel with the highest amplitude of ripple oscillations (100-250 Hz band) and associated spiking activity. Neurons
692 recorded dorsal of the channel with the highest SWR power were characterized as deep CA1 pyramidal neurons⁸¹.
693 Conversely, neurons recorded ventrally of this reference channel were characterized as superficial CA1 pyramidal neurons.
694 Given that neuronal spikes can be identified in more than one channel of the polytrode, neurons were assigned to the
695 channel with the highest spike amplitude³⁰. Well-described CSD profiles of hippocampal oscillatory patterns were used to
696 assign somatodendritic CA1 and DG layers to channels (**Supplementary Fig. 5e**). The middle of stratum radiatum was
697 assigned to the channel with the deepest sharp wave current-source density sink associated with ripple oscillations^{20,134}.
698 Stratum oriens was defined as the channels above the pyramidal layer SWR CSD source and below the internal capsule,
699 characterized by a positive component of the sharp-waves. For the identification of DG layers, we used the CSD and
700 amplitude versus depth profile of dentate spikes (DS)¹⁰. DS are large-amplitude events that occur naturally during offline
701 states and reflect synchronized bursts of medial and lateral entorhinal cortex¹⁰. The outer molecular layer was defined
702 as the Type-I dentate spike (DSI) sink, while the middle molecular layer was assigned as the channels exhibiting DSII
703 sinks. The inner molecular layer was defined as the channel of the deepest secondary sink in the SWR triggered CSD,
704 which is ventral of the DSII middle molecular layer sink. The source of DSII spikes, which corresponds to a typically
705 more localized source preceding SWR events¹³⁴, together with the polarity reversal of the DSII, which occurs above
706 the granule cell layer¹⁰, enables the precise detection of this layer¹⁰⁶. Stratum CA1 lacunosum-moleculare was defined
707 as the difference between the theta-trough triggered CSD sink and the outer molecular DSII sink. This corresponds to
708 approximately the dorsal third of the theta sink. For V1 CSD, layers were assigned based on known profiles during visual
709 stimulation. An early sink following visual stimulation between layers 3 and 4⁸⁰, a later sink between layers 5 and 6, and
710 a peak of the high-frequency power in mid-layer 5^{103,107}.

Network event detection

711 Ripples were detected from a CA1 pyramidal layer channel using the instantaneous amplitude of the analytic signal
712 calculated from the band-pass filtered (80-250 Hz). The instantaneous amplitude was referenced to the amplitude of a
713 channel typically from the cortex overlying the hippocampus, was convolved with a Gaussian kernel (100 ms, 12 ms
714 s.d.) and normalized. The mean and s.d. of the referenced amplitude were calculated for periods of quiescent immobility
715 and slow-wave sleep. Ripples were detected as events exceeding 3 s.d with a minimum duration of 4 cycles and were
716 aligned on the deepest trough of the band-pass filtered signal. Gamma bursts were detected using a similar procedure,
717 but for the relevant frequency band and behavioral states. Dentate spikes (DS) were detected as large deviations (>3
718 s.d.) of the envelope of the 2-50 Hz band-pass filtered LFP signal from the DG hilar region (using the channel from the
719 hilar region with the peak amplitude), referenced to the CA1 pyramidal layer. DS were detected from the subtracted
720 envelopes of the two channels. The trigger time for the calculation of the DS CSDs was the peak of this bandpass

721 amplitude. Following detection, DS were clustered in two types using k-means clustering on the 2D space defined by the
722 2 principal components of the CA1/DG depth profile of each spike. The classification between the two types was based
723 on the PCA of the translaminar LFP profile of the detected events. UP and DOWN states were detected by binning the
724 spike train for every single unit in 10 ms windows, normalized, and convolved with a 0.5 s wide, 20 ms s.d. Gaussian
725 kernel. The average binned spike histogram was calculated across all simultaneously recorded cells (including PNs and
726 INs). DOWN states were detected as periods longer than 50 ms with no spikes across all the cells and the exact onset
727 and offset of DOWN states were detected. UP states were detected as periods contained between two DOWN states,
728 lasting between 100 ms and 2000 ms, with the average MUA activity during this period exceeding the 70th percentile of
729 the MUA activity throughout the recording.

Single-unit analysis and classification

730 Raw data were processed to detect spikes and extract single-unit activity. Briefly, the wide-band signals were band-pass
731 filtered (0.6 kHz-6 kHz), spatially whitened across channels and thresholded and putative spikes were isolated. Clustering
732 was performed using template matching algorithms implemented in Kilosort²⁹ the ISO-SPLIT method implemented in
733 MountainSort package²⁶ and computed cluster metrics were used to pre-select units for later manual curation. Specifically,
734 only clusters with low overlap with noise (<0.05), low peak noise (<30), and high isolation index (>0.9) were considered
735 for manual curation, using custom-written software. At the manual curation step, only units with clean interspike interval
736 (ISI) period, clean waveform, and sufficient amplitude were selected for further analysis. For the data collected with high-
737 density polytrodes, after manual curation, a template of the spike waveform across 10 geometrically adjacent channels was
738 calculated and the unit was re-assigned to the channel with the largest waveform amplitude. To classify single-units into
739 putative excitatory and inhibitory cells, a set of parameters based on the waveform shape, firing rate, and autocorrelogram
740 were calculated. The two parameters that offered the best separation, in accordance to what has been reported in the
741 past, were the trough-to-peak duration⁶ and the spike-asymmetry index (the difference between the pre- and post-
742 depolarization positive peaks of the filtered trace)²⁹, reflecting the duration of action potential repolarization which
743 is shorter for interneurons^{41,48} (**Supplementary Fig. 3a,b**). Single-units with <200 spikes in the periods of interest
744 were excluded from all analyses. Spike trains were z-scored across all periods analyzed (typically quiescence and sleep
745 periods unless otherwise specified). Dimensionality-reduction was performed on the inspiration-triggered activity and
746 correlation matrix using PCA. Isomap and other dimensionality techniques were implemented using the Matlab Toolbox
747 for Dimensionality Reduction. Importantly, the results were qualitatively independent of the particular dimensionality-
748 reduction method used (**Supplementary Fig. 4c**). Co-firing index for each pair of units was defined as the mean ratio
749 of co-occurring spikes to the total number of spikes for both units for each 10ms bin (**Fig. 7f**). For the ripple and opto-
750 ripple evoked response analyses, triggered spike-trains were normalized across events, neurons, and breathing phase, in
751 order to account for intrinsic firing rate differences across cells and breathing phase (**Fig. 7e,i,s; Supplementary Fig.**
752 **8i**).

Optogenetics

753 For the generation of opto-ripples, mice were unilaterally injected with 300nL of AAV2/9-CaMKIIa-
754 ChETA(E123T/H134R)-eYFP-WPRE.hGH in the dCA1 region (AP: -2.3 mm, ML: 1.5 mm, DV: 1.2) using positive
755 pressure through glass pipettes (tip diameter 20 – 30 μ m) connected to a Picospritzer. Three weeks after the injection,
756 the functional effect of the opsin was tested in the awake head-fixed mouse using electrophysiological recordings from
757 the dCA1 using a silicone probe coupled with a 200 μ m diameter optic fiber. 465nm light was delivered using LEDs
758 (Plexon) and the intensity was calibrated to generate opto-ripples (**Fig. 7m**) of amplitude similar to the intrinsically
759 recorded oscillation (typically 25 – 50mW/mm²). The stimulation pattern was selected to be a half-sine wave with 200ms
760 duration in order to generate opto-ripples as previously described^{37,115} with duration and characteristics similar to the
761 intrinsic ripples. After this process, an optic fiber was chronically implanted at the same coordinates and electrophysi-
762 ological recordings from the prefrontal cortex were performed while generating opto-ripples in the dCA1. Stimulations
763 were delivered with random inter-stimulation intervals (1 - 3 s) and were later analyzed as a function of the respiration
764 phase during which they were delivered.

Pharmacology

765 To causally prove the role of respiratory epithelium neurons in driving oscillations in the prefrontal cortex of mice, we
766 induced selective degeneration of the olfactory epithelium cells (**Supplementary Fig. 7a**) by systemic administration
767 of methimazole⁸. Mice were injected intraperitoneally with methimazole (75 mg/kg). The effect on neuronal dynamics
768 was characterized at 3, 7, or 10 days following the ablation of OSNs, with no appreciable differences between these
769 timepoints.

Statistical analysis

770 For statistical analyses, the normality assumption of the underlying distributions was assessed using the Kolmogorov-
771 Smirnov test, Lilliefors test, and Shapiro-Wilk tests. Further, homoscedasticity was tested using the Levene or
772 Brown-Forsythe tests. If the tests rejected their respective null hypothesis non-parametric statistics were used, alter-
773 natively, parametric tests were performed. When multiple statistical tests were performed, Bonferroni corrections were
774 applied. Where necessary, resampling methods such as bootstrap and permutation tests were used to properly quantify
775 significance. For box plots, the middle, bottom, and top lines correspond to the median, bottom, and top quartile, and
776 whiskers to lower and upper extremes minus bottom quartile and top quartile, respectively.

Data availability

777 All relevant data that support the findings of this study will be made available from the corresponding authors upon
778 reasonable request.

Code availability

779 Custom code used to acquire, process, and analyze these data is available online (DataSuite, Nikolaos Karalis; [https:](https://github.com/nikolaskaralis/data_suite)
780 [//github.com/nikolaskaralis/data_suite](https://github.com/nikolaskaralis/data_suite)).

References

1. Acsády, L., Kamondi, A., Sik, A., Freund, T. & Buzsáki, G. GABAergic Cells Are the Major Postsynaptic Targets of Mossy Fibers in the Rat Hippocampus. *Journal of Neuroscience* *18*, 3386–403 (1998).
 2. Adrian, E.D. Olfactory Reactions in the Brain of the Hedgehog. *The Journal of Physiology* *100*, 459–473 (1942).
 3. Adrian, E. The Electrical Activity of the Mammalian Olfactory Bulb. *Electroencephalography and Clinical Neurophysiology* *2*, 377–388 (1950).
 4. Arzi, A. *et al.* Humans Can Learn New Information during Sleep. *Nature Neuroscience* (2012).
 5. Barnett, L. & Seth, A.K. The MVGC Multivariate Granger Causality Toolbox: A New Approach to Granger-Causal Inference. *Journal of Neuroscience Methods* *223*, 50–68 (2014).
 6. Bartho, P. Characterization of Neocortical Principal Cells and Interneurons by Network Interactions and Extracellular Features. *Journal of Neurophysiology* *92*, 600–608 (2004).
 7. Battaglia, F.P., Benchenane, K., Sirota, A., Pennartz, C.M. & Wiener, S.I. The Hippocampus: Hub of Brain Network Communication for Memory. *Trends in Cognitive Sciences* (2011).
 8. Bergman, U., Ostergren, A., Gustafson, A.-L. & Brittebo, B. Differential Effects of Olfactory Toxicants on Olfactory Regeneration. *Archives of toxicology* *76*, 104–112 (2002).
 9. Biskamp, J., Bartos, M. & Sauer, J.F. Organization of Prefrontal Network Activity by Respiration-Related Oscillations. *Scientific Reports* *7*, 45508–45508 (2017).
 10. Bragin, A., Jandó, G., Nádasdy, Z., Hetke, J., Wise, K. & Buzsáki, G. Gamma (40–100 Hz) Oscillation in the Hippocampus of the Behaving Rat. *The Journal of Neuroscience: The Official Journal of the Society for Neuroscience* *15*. 01425, 47–60 (1 Pt 1 1995).
 11. Brankač, J., Stewart, M. & E. Fox, S. Current Source Density Analysis of the Hippocampal Theta Rhythm: Associated Sustained Potentials and Candidate Synaptic Generators. *Brain Research* *615*, 310–327 (1993).
 12. Brown, R.P. & Gerbarg, P.L. Sudarshan Kriya Yogic Breathing in the Treatment of Stress, Anxiety, and Depression: Part I—Neurophysiologic Model. *The Journal of Alternative and Complementary Medicine* *11*, 189–201 (2005).
 13. Buzsáki, G. Memory Consolidation during Sleep: A Neurophysiological Perspective. *Journal of sleep research* *7 Suppl 1*, 17–23 (1998).
 14. Buzsáki, G. Two-Stage Model of Memory Trace Formation: A Role for "Noisy" Brain States. *Neuroscience* *31*, 551–570 (1989).
 15. Buzsáki, G. Theta Oscillations in the Hippocampus. *Neuron* *33*, 325–340 (2002).
 16. Buzsáki, G. *Rhythms of the Brain* 1 p. ([Oxford University Press, 2006]).
 17. Buzsáki, G. Neural Syntax: Cell Assemblies, Synapsembles, and Readers. *Neuron* *68*, 362–385 (2010).
 18. Buzsáki, G. György Buzsáki. *Current Biology* *23*, R983–r985 (2013).
 19. Buzsáki, G. & Bland, B.H. Obituary: Cornelius H. Vanderwolf. *Hippocampus* *25*, 1191–1192 (2015).
 20. Buzsáki, G., Lai-Wo S., L. & Vanderwolf, C.H. Cellular Bases of Hippocampal EEG in the Behaving Rat. *Brain Research Reviews* *6*, 139–171 (1983).
 21. Buzsáki, G. *et al.* Tools for Probing Local Circuits: High-Density Silicon Probes Combined with Optogenetics. *Neuron* *86*, 92–105 (2015).
 22. Carmichael, J.E., Gmaz, J.M. & van der Meer, M.A. Gamma Oscillations in the Rat Ventral Striatum Originate in the Piriform Cortex. *The Journal of Neuroscience* *37*, 7962–7974 (2017).
 23. Carr, M.F., Jadhav, S.P. & Frank, L.M. Hippocampal Replay in the Awake State: A Potential Substrate for Memory Consolidation and Retrieval. *Nature Neuroscience* *14*, 147–153 (2011).
 24. Chang, R.B., Strohlic, D.E., Williams, E.K., Umans, B.D. & Liberles, S.D. Vagal Sensory Neuron Subtypes That Differentially Control Breathing. *Cell* *161*, 622–633 (2015).
 25. Chauvette, S., Volgushev, M. & Timofeev, I. Origin of Active States in Local Neocortical Networks during Slow Sleep Oscillation. *Cerebral Cortex* *20*, 2660–2674 (2010).
 26. Chung, J.E. *et al.* A Fully Automated Approach to Spike Sorting. *Neuron* *95*, 1381–1394.e6 (2017).
 27. Courtin, J. *et al.* Prefrontal Parvalbumin Interneurons Shape Neuronal Activity to Drive Fear Expression. *Nature* *505*, 92–96 (2014).
 28. Crapse, T.B. & Sommer, M.A. Corollary Discharge across the Animal Kingdom. *Nature Reviews Neuroscience* *9*, 587–600 (2008).
 29. Csicsvari, J., Hirase, H., Czurko, A. & Buzsáki, G. Reliability and State Dependence of Pyramidal Cell-Interneuron Synapses in the Hippocampus: An Ensemble Approach in the Behaving Rat. *Neuron* *21*, 179–189 (1998).
 30. Csicsvari, J., Jamieson, B., Wise, K.D. & Buzsáki, G. Mechanisms of Gamma Oscillations in the Hippocampus of the Behaving Rat. *Neuron* *37*, 311–322 (2003).
 31. Dejean, C. *et al.* Prefrontal Neuronal Assemblies Temporally Control Fear Behaviour. *Nature* *535*, 420–424 (2016).
 32. Del Negro, C.A., Funk, G.D. & Feldman, J.L. Breathing Matters. *Nature Reviews Neuroscience* *19*, 351–367 (2018).
-

-
33. DiCarlo, J.J., Lane, J.W., Hsiao, S.S. & Johnson, K.O. Marking Microelectrode Penetrations with Fluorescent Dyes. *Journal of Neuroscience Methods* *64*, 75–81 (1996).
 34. Euston, D.R., Tatsuno, M. & McNaughton, B.L. Fast-Forward Playback of Recent Memory Sequences in Prefrontal Cortex during Sleep. *Science* *318*, 1147–1150 (2007).
 35. Ferguson, J.E., Boldt, C. & Redish, A.D. Creating Low-Impedance Tetrodes by Electroplating with Additives. *Sensors and Actuators, A: Physical* *156*, 388–393 (2009).
 36. Fernandez-Ruiz, A., Munoz, S., Sancho, M., Makarova, J., Makarov, V.A. & Herreras, O. Cytoarchitectonic and Dynamic Origins of Giant Positive Local Field Potentials in the Dentate Gyrus. *Journal of Neuroscience* *33*, 15518–15532 (2013).
 37. Fernández-Ruiz, A., Oliva, A., Fermino de Oliveira, E., Rocha-Almeida, F., Tingley, D. & Buzsáki, G. Long-Duration Hippocampal Sharp Wave Ripples Improve Memory. *Science* *364*, 00005, 1082–1086 (2019).
 38. Fischer, I. *et al.* Zero-Lag Long-Range Synchronization via Dynamical Relaying. *Physical Review Letters* *97*, 123902–123902 (2006).
 39. Fontanini, A., Spano, P. & Bower, J.M. Ketamine–Xylazine-Induced Slow (~ 1.5 Hz) Oscillations in the Rat Piriform (Olfactory) Cortex Are Functionally Correlated with Respiration. *Journal of Neuroscience* *23*, 7993–8001 (2003).
 40. Freeman, J.A. & Nicholson, C. Experimental Optimization of Current Source-Density Technique for Anuran Cerebellum. *Journal of neurophysiology* *38*, 369–382 (1975).
 41. Freund, T.F. & Buzsáki, G. Interneurons of the Hippocampus. *Hippocampus* *6*, 347–470 (1996).
 42. Fukunaga, I., Herb, J.T., Kollo, M., Boyden, E.S. & Schaefer, A.T. Independent Control of Gamma and Theta Activity by Distinct Interneuron Networks in the Olfactory Bulb. *Nature Neuroscience* *17*, 1208–1216 (2014).
 43. Girardeau, G., Inema, I. & Buzsáki, G. Reactivations of Emotional Memory in the Hippocampus–Amygdala System during Sleep. *Nature Neuroscience* *20*, 1634–1642 (2017).
 44. Girardeau, G. *et al.* Selective Suppression of Hippocampal Ripples Impairs Spatial Memory. *Nature Neuroscience* *12*, 1222–1223 (2009).
 45. Gold, A.R. Functional Somatic Syndromes, Anxiety Disorders and the Upper Airway: A Matter of Paradigms. *Sleep Medicine Reviews* *15*, 389–401 (2011).
 46. Grosmaître, X., Santarelli, L.C., Tan, J., Luo, M. & Ma, M. Dual Functions of Mammalian Olfactory Sensory Neurons as Odor Detectors and Mechanical Sensors. *Nature Neuroscience* *10*, 348–354 (2007).
 47. Hazan, L., Zugaro, M. & Buzsáki, G. Klusters, NeuroScope, NDManager: A Free Software Suite for Neurophysiological Data Processing and Visualization. *Journal of Neuroscience Methods* *155*, 207–216 (2006).
 48. Henze, D.A., Borhegyi, Z., Csicsvari, J., Mamiya, A., Harris, K.D. & Buzsáki, G. Intracellular Features Predicted by Extracellular Recordings in the Hippocampus In Vivo. *Journal of Neurophysiology* *84*, 390–400 (2000).
 49. Herry, C. & Johansen, J.P. Encoding of Fear Learning and Memory in Distributed Neuronal Circuits. *Nature Neuroscience* *17*, 1644–1654 (2014).
 50. Hoover, W.B. & Vertes, R.P. Anatomical Analysis of Afferent Projections to the Medial Prefrontal Cortex in the Rat. *Brain Structure and Function* *212*, 149–179 (2007).
 51. Isomura, Y. *et al.* Integration and Segregation of Activity in Entorhinal-Hippocampal Subregions by Neocortical Slow Oscillations. *Neuron* *52*, 871–882 (2006).
 52. Isosaka, T. *et al.* Htr2a-Expressing Cells in the Central Amygdala Control the Hierarchy between Innate and Learned Fear. *Cell* *163*, 1153–1164 (2015).
 53. Ito, J. *et al.* Whisker Barrel Cortex Delta Oscillations and Gamma Power in the Awake Mouse Are Linked to Respiration. *Nature Communications* *5* (2014).
 54. Jadhav, S.P., Kemere, C., German, P.W. & Frank, L.M. Awake Hippocampal Sharp-Wave Ripples Support Spatial Memory. *Science* *336*, 1454–1458 (2012).
 55. Jadhav, S.P.P., Rothschild, G., Roumis, D.K.K. & Frank, L.M.M. Coordinated Excitation and Inhibition of Prefrontal Ensembles during Awake Hippocampal Sharp-Wave Ripple Events. *Neuron* *90*, 113–127 (2016).
 56. Ji, D. & Wilson, M.A. Coordinated Memory Replay in the Visual Cortex and Hippocampus during Sleep. *Nature Neuroscience* *10*, 100–107 (2007).
 57. Karalis, N. *et al.* 4-Hz Oscillations Synchronize Prefrontal–Amygdala Circuits during Fear Behavior. *Nature Neuroscience* *19*, 605–612 (2016).
 58. Kay, L.M. & Freeman, W.J. Bidirectional Processing in the Olfactory–Limbic Axis during Olfactory Behavior. *Behavioral Neuroscience* *112*, 541–553 (1998).
 59. Khodagholy, D., Gelineas, J.N. & Buzsáki, G. Learning-Enhanced Coupling between Ripple Oscillations in Association Cortices and Hippocampus. *Science* *358*, 369–372 (2017).
 60. Kitamura, T. *et al.* Engrams and Circuits Crucial for Systems Consolidation of a Memory. *Science* *356*, 73–78 (2017).
 61. Kumar, A., Rotter, S. & Aertsen, A. Spiking Activity Propagation in Neuronal Networks: Reconciling Different Perspectives on Neural Coding. *Nature Reviews Neuroscience* *11*, 615–627 (2010).
 62. Kunik, M.E. *et al.* Surprisingly High Prevalence of Anxiety and Depression in Chronic Breathing Disorders. *Chest* *127*, 1205–1211 (2005).
-

-
63. Lee, A.K. & Wilson, M.A. Memory of Sequential Experience in the Hippocampus during Slow Wave Sleep. *Neuron* *36*, 1183–1194 (2002).
64. Leitner, F.C. *et al.* Spatially Segregated Feedforward and Feedback Neurons Support Differential Odor Processing in the Lateral Entorhinal Cortex. *Nature Neuroscience* *19*, 935–944 (2016).
65. Lemieux, M., Chauvette, S. & Timofeev, I. Neocortical Inhibitory Activities and Long-Range Afferents Contribute to the Synchronous Onset of Silent States of the Neocortical Slow Oscillation. *Journal of Neurophysiology* *113*, 768–779 (2015).
66. Lepousez, G. & Lledo, P.-M. Odor Discrimination Requires Proper Olfactory Fast Oscillations in Awake Mice. *Neuron* *80*, 1010–1024 (2013).
67. Liu, Y., Rodenkirch, C., Moskowitz, N., Schriver, B. & Wang, Q. Dynamic Lateralization of Pupil Dilation Evoked by Locus Coeruleus Activation Results from Sympathetic, Not Parasympathetic, Contributions. *Cell Reports* *20*, 3099–3112 (2017).
68. Lockmann, A.L.V., Laplagne, D.A., Leão, R.N. & Tort, A.B.L. A Respiration-Coupled Rhythm in the Rat Hippocampus Independent of Theta and Slow Oscillations. *The Journal of Neuroscience* *36*, 5338–5352 (2016).
69. Logothetis, N.K., Kayser, C. & Oeltermann, A. In Vivo Measurement of Cortical Impedance Spectrum in Monkeys: Implications for Signal Propagation. *Neuron* *55*, 809–823 (2007).
70. Lopes, G.A. *et al.* Bonsai: An Event-Based Framework for Processing and Controlling Data Streams. *Frontiers in Neuroinformatics* *9* (2015).
71. Ludwig, K.A., Langhals, N.B., Joseph, M.D., Richardson-Burns, S.M., Hendricks, J.L. & Kipke, D.R. Poly(3,4-Ethylenedioxythiophene) (PEDOT) Polymer Coatings Facilitate Smaller Neural Recording Electrodes. *Journal of Neural Engineering* *8* (2011).
72. Macrides, F. & Chorover, S.L. Olfactory Bulb Units: Activity Correlated with Inhalation Cycles and Odor Quality. *Science* *175*, 84–87 (1972).
73. Maingret, N., Girardeau, G., Todorova, R., Goutierre, M. & Zugaro, M. Hippocampo-Cortical Coupling Mediates Memory Consolidation during Sleep. *Nature Neuroscience* *19*, 959–964 (2016).
74. Martín-Vázquez, G., Makarova, J., Makarov, V.A. & Herreras, O. Determining the True Polarity and Amplitude of Synaptic Currents Underlying Gamma Oscillations of Local Field Potentials. *PLoS ONE* *8* (ed Barnes, G.R.) e75499 (2013).
75. Masimore, B., Kakalios, J. & Redish, A. Measuring Fundamental Frequencies in Local Field Potentials. *Journal of Neuroscience Methods* *138*, 97–105 (2004).
76. Massimini, M., Huber, R., Ferrarelli, F., Hill, S. & Tononi, G. The Sleep Slow Oscillation as a Traveling Wave. *Journal of Neuroscience* *24*, 6862–6870 (2004).
77. Maviel, T., Durkin, T.P., Menzaghi, F. & Bontempi, B. Sites of Neocortical Reorganization Critical for Remote Spatial Memory. *Science* *305*, 96–99 (2004).
78. McGaugh, J.L. Memory - A Century of Consolidation. *Science* *287*, 248–251 (2000).
79. Mitra, P.P. & Pesaran, B. Analysis of Dynamic Brain Imaging Data. *Biophysical Journal* *76*, 691–708 (1999).
80. Mitzdorf, U. Properties of the Evoked Potential Generators: Current Source-Density Analysis of Visually Evoked Potentials in the Cat Cortex. *International Journal of Neuroscience* *33*, 33–59 (1987).
81. Mizuseki, K., Diba, K., Pastalkova, E. & Buzsáki, G. Hippocampal CA1 Pyramidal Cells Form Functionally Distinct Sublayers. *Nature Neuroscience* *14*, 1174–1183 (2011).
82. Mizuseki, K., Sirota, A., Pastalkova, E. & Buzsáki, G. Theta Oscillations Provide Temporal Windows for Local Circuit Computation in the Entorhinal-Hippocampal Loop. *Neuron* *64*, 267–280 (2009).
83. Moberly, A.H., Schreck, M., Bhattarai, J.P., Zweifel, L.S., Luo, W. & Ma, M. Olfactory Inputs Modulate Respiration-Related Rhythmic Activity in the Prefrontal Cortex and Freezing Behavior. *Nature Communications* *9* (2018).
84. Moore, J.D. *et al.* Hierarchy of Orofacial Rhythms Revealed through Whisking and Breathing. *Nature* *497*, 205–210 (2013).
85. Morgane, P.J., Galler, J.R. & Mokler, D.J. A Review of Systems and Networks of the Limbic Forebrain/Limbic Midbrain. *Progress in Neurobiology* *75*, 143–160 (2005).
86. Neuman, A. *et al.* Dyspnea in Relation to Symptoms of Anxiety and Depression: A Prospective Population Study. *Respiratory Medicine* *100*, 1843–1849 (2006).
87. Nguyen Chi, V. *et al.* Hippocampal Respiration-Driven Rhythm Distinct from Theta Oscillations in Awake Mice. *Journal of Neuroscience* *36*, 162–177 (2016).
88. Nicholson, C. & Freeman, J.A. Theory of Current Source-Density Analysis and Determination of Conductivity Tensor for Anuran Cerebellum. *Journal of Neurophysiology* *38*, 356–368 (1975).
89. Nonomura, K. *et al.* Piezo2 Senses Airway Stretch and Mediates Lung Inflation-Induced Apnoea. *Nature* *541*, 176–181 (2017).
90. O’Neill, J., Pleydell-Bouverie, B., Dupret, D. & Csicsvari, J. Play It Again: Reactivation of Waking Experience and Memory. *Trends in Neurosciences* *33*, 220–229 (2010).
-

-
- 91.Ottoson, D. Analysis of the Electrical Activity of the Olfactory Epithelium. *Acta physiologica Scandinavica. Supplementum 35*, 1–83 (1955).
- 92.Pachitariu, M., Steinmetz, N., Kadir, S., Carandini, M. & Harris, K.D. Kilosort: Realtime Spike-Sorting for Extracellular Electrophysiology with Hundreds of Channels. *bioRxiv* (2016).
- 93.Paxinos, G. & Franklin, K.B.J. *The Mouse Brain in Stereotaxic Coordinates* 00122. 140 pp. ([Gulf Professional Publishing, 2004]).
- 94.Pennartz, C.M.A. The Ventral Striatum in Off-Line Processing: Ensemble Reactivation during Sleep and Modulation by Hippocampal Ripples. *Journal of Neuroscience* *24*, 6446–6456 (2004).
- 95.Pennartz, C.M.A., Ito, R., Verschure, P.F.M.J., Battaglia, F.P. & Robbins, T.W. The Hippocampal-Striatal Axis in Learning, Prediction and Goal-Directed Behavior. *Trends in Neurosciences* *34*, 548–559 (2011).
- 96.Perl, O. *et al.* Odors Enhance Slow-Wave Activity in Non-Rapid Eye Movement Sleep. *Journal of Neurophysiology* *115*, 2294–2302 (2016).
- 97.Pettersen, K.H., Devor, A., Ulbert, I., Dale, A.M. & Einevoll, G.T. Current-Source Density Estimation Based on Inversion of Electrostatic Forward Solution: Effects of Finite Extent of Neuronal Activity and Conductivity Discontinuities. *Journal of Neuroscience Methods* *154*, 116–133 (2006).
- 98.Peyrache, A., Battaglia, F.P. & Destexhe, A. Inhibition Recruitment in Prefrontal Cortex during Sleep Spindles and Gating of Hippocampal Inputs. *Proceedings of the National Academy of Sciences* *108*, 17207–17212 (2011).
- 99.Peyrache, A., Khamassi, M., Benchenane, K., Wiener, S.I. & Battaglia, F.P. Replay of Rule-Learning Related Neural Patterns in the Prefrontal Cortex during Sleep. *Nature Neuroscience* *12*, 919–926 (2009).
- 100.Phillips, M.E., Sachdev, R.N.S., Willhite, D.C. & Shepherd, G.M. Respiration Drives Network Activity and Modulates Synaptic and Circuit Processing of Lateral Inhibition in the Olfactory Bulb. *Journal of Neuroscience* *32*, 85–98 (2012).
- 101.Ranck, J.B. Specific Impedance of Rabbit Cerebral Cortex. *Experimental neurology* *7*, 144–152 (1963).
- 102.Rasch, B., Büchel, C., Gais, S. & Born, J. Odor Cues during Slow-Wave Sleep Prompt Declarative Memory Consolidation. *Science* *315*, 1426–1429 (2007).
- 103.Ray, S. & Maunsell, J.H.R. Differences in Gamma Frequencies across Visual Cortex Restrict Their Possible Use in Computation. *Neuron* *67*. 00322, 885–896 (2010).
- 104.Rothschild, G., Eban, E. & Frank, L.M. A Cortical–Hippocampal–Cortical Loop of Information Processing during Memory Consolidation. *Nature Neuroscience* *20*, 251–259 (2017).
- 105.Sanchez-Vives, M.V. & McCormick, D.A. Cellular and Network Mechanisms of Rhythmic Recurrent Activity in Neocortex. *Nature Neuroscience* *3*, 1027–1034 (2000).
- 106.Senzai, Y. & Buzsáki, G. Physiological Properties and Behavioral Correlates of Hippocampal Granule Cells and Mossy Cells. *Neuron* *93*, 691–704.e5 (2017).
- 107.Senzai, Y., Fernandez-Ruiz, A. & Buzsáki, G. Layer-Specific Physiological Features and Interlaminar Interactions in the Primary Visual Cortex of the Mouse. *Neuron* *101*, 500–513.e5 (2019).
- 108.Shu, Y., Hasenstaub, A. & McCormick, D.A. Turning on and off Recurrent Balanced Cortical Activity. *Nature* *423*, 288–293 (2003).
- 109.Siapas, A.G., Lubenov, E.V. & Wilson, M.A. Prefrontal Phase Locking to Hippocampal Theta Oscillations. *Neuron* *46*, 141–151 (2005).
- 110.Siapas, A.G. & Wilson, M.A. Coordinated Interactions between Hippocampal Ripples and Cortical Spindles during Slow-Wave Sleep. *Neuron* *21*, 1123–1128 (1998).
- 111.Sirota, A., Csicsvari, J., Buhl, D.L. & Buzsaki, G. Communication between Neocortex and Hippocampus during Sleep in Rodents. *Proceedings of the National Academy of Sciences* *100*, 2065–2069 (2003).
- 112.Sirota, A. & Buzsáki, G. Interaction between Neocortical and Hippocampal Networks via Slow Oscillations. *Thalamus and Related Systems* *3*, 245 (2005).
- 113.Sirota, A., Montgomery, S., Fujisawa, S., Isomura, Y., Zugaro, M.B. & Buzsaki, G. Entrainment of Neocortical Neurons and Gamma Oscillations by the Hippocampal Theta Rhythm. *Neuron* *60*, 683–697 (2008).
- 114.Squire, L.R. "Memory and the Hippocampus: A Synthesis from Findings with Rats, Monkeys, and Humans": Correction. *Psychological Review* *99*, 582–582 (1992).
- 115.Stark, E., Roux, L., Eichler, R., Senzai, Y., Royer, S. & Buzsaki, G. Pyramidal Cell-Interneuron Interactions Underlie Hippocampal Ripple Oscillations. *Neuron* *83*, 467–480 (2014).
- 116.Steriade, M.M., Amzica, F & Nuñez, A. Cholinergic and Noradrenergic Modulation of the Slow (Approximately 0.3 Hz) Oscillation in Neocortical Cells. *Journal of Neurophysiology* *70*, 1385–1400 (1993).
- 117.Straka, H., Simmers, J. & Chagnaud, B.P. A New Perspective on Predictive Motor Signaling. *Current Biology* *28*, R193–r194 (2018).
- 118.Stujenske, J.M., Likhtik, E., Topiwala, M.A. & Gordon, J.A. Fear and Safety Engage Competing Patterns of Theta-Gamma Coupling in the Basolateral Amygdala. *Neuron* *83*, 919–933 (2014).
- 119.Sullivan, D., Csicsvari, J., Mizuseki, K., Montgomery, S., Diba, K. & Buzsáki, G. Relationships between Hippocampal Sharp Waves, Ripples, and Fast Gamma Oscillation: Influence of Dentate and Entorhinal Cortical Activity. *The Journal of neuroscience : the official journal of the Society for Neuroscience* *31*, 8605–16 (2011).
-

-
120. Summerlee, A.J.S., Paisley, A.C. & Goodall, C.L. A Method for Determining the Position of Chronically Implanted Platinum Microwire Electrodes. *Journal of Neuroscience Methods* *5*, 7–11 (1982).
 121. Timofeev, I., Grenier, F. & Steriade, M.M. Impact of Intrinsic Properties and Synaptic Factors on the Activity of Neocortical Networks in Vivo. In *Journal of Physiology*, **94**. ([2000]), 343–355.
 122. Tort, A.B.L. *et al.* Dynamic Cross-Frequency Couplings of Local Field Potential Oscillations in Rat Striatum and Hippocampus during Performance of a T-Maze Task. *Proceedings of the National Academy of Sciences* *105*, 20517–20522 (2008).
 123. Tort, A.B., Ponsel, S., Jessberger, J., Yanovsky, Y., Brankač, J. & Draguhn, A. Parallel Detection of Theta and Respiration-Coupled Oscillations throughout the Mouse Brain. *Scientific Reports* *8*, 1–14 (2018).
 124. Valero, M. *et al.* Determinants of Different Deep and Superficial CA1 Pyramidal Cell Dynamics during Sharp-Wave Ripples. *Nature Neuroscience* *18*, 1281–1290 (2015).
 125. Vanderwolf, C. Hippocampal Activity, Olfaction, and Sniffing: An Olfactory Input to the Dentate Gyrus. *Brain Research* *593*, 197–208 (1992).
 126. Viczko, J., Sharma, A.V., Pagliardini, S., Wolansky, T. & Dickson, C.T. Lack of Respiratory Coupling with Neocortical and Hippocampal Slow Oscillations. *Journal of Neuroscience* *34*, 3937–3946 (2014).
 127. Vinck, M. *et al.* How to Detect the Granger-Causal Flow Direction in the Presence of Additive Noise? *NeuroImage* *108*, 301–318 (2015).
 128. Vyazovskiy, V.V., Olcese, U., Hanlon, E.C., Nir, Y., Cirelli, C. & Tononi, G. Local Sleep in Awake Rats. *Nature* *472*, 443–447 (2011).
 129. Wilson, M. & McNaughton, B. Dynamics of the Hippocampal Ensemble Code for Space. *Science* *261*, 1055–1058 (1993).
 130. Yackle, K. *et al.* Breathing Control Center Neurons That Promote Arousal in Mice. *Science* *355*, 1411–1415 (2017).
 131. Yang, L., Lee, K., Villagrancia, J. & Masmanidis, S.C. Open Source Silicon Microprobes for High Throughput Neural Recording. *Journal of Neural Engineering* *17*, 016036 (2020).
 132. Yang, Y. *et al.* Ketamine Blocks Bursting in the Lateral Habenula to Rapidly Relieve Depression. *Nature* *554*, 317–322 (2018).
 133. Yanovsky, Y., Ciatipis, M., Draguhn, A., Tort, A.B.L. & Brankač, J. Slow Oscillations in the Mouse Hippocampus Entrained by Nasal Respiration. *Journal of Neuroscience* *34*, 5949–5964 (2014).
 134. Ylinen, A., Soltész, I., Bragin, A., Penttonen, M., Sik, A. & Buzsáki, G. Intracellular Correlates of Hippocampal Theta Rhythm in Identified Pyramidal Cells, Granule Cells, and Basket Cells. *Hippocampus* *5*, 78–90 (1995).
 135. Zelano, C. *et al.* Nasal Respiration Entrain Human Limbic Oscillations and Modulates Cognitive Function. *The Journal of Neuroscience* *36*, 12448–12467 (2016).
 136. Zhong, W. *et al.* Selective Entrainment of Gamma Subbands by Different Slow Network Oscillations. *Proceedings of the National Academy of Sciences* *114*, 4519–4524 (2017).

Figures

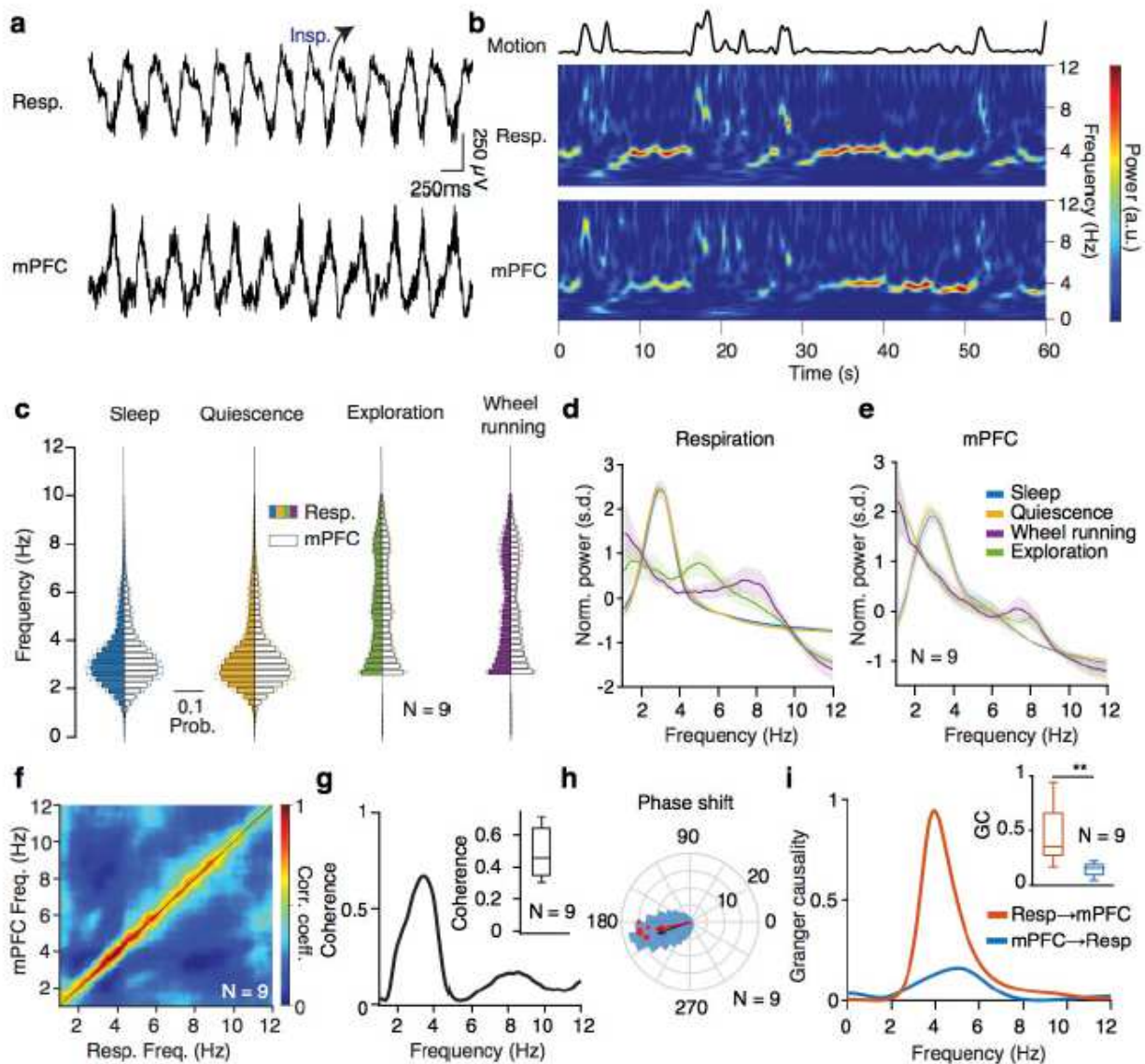


Figure 1

Prefrontal oscillations are related to breathing throughout behavioral states. (a) Example traces of simultaneously recorded respiratory EOG and medial prefrontal local field potentials (LFP) (See also Supplementary Fig. 1). (b) Example time-frequency decomposition of respiratory and mPFC LFP signals, revealing the reliable relationship between the two signals. (c) Distribution of peak frequency bins of the spectrally decomposed respiration (left; darker colors) and mPFC LFP (right; lighter colors) during slow-wave sleep, quiescence, exploratory behavior and self-initiated wheel running (N = 9 freely-behaving mice) (See also Supplementary Fig. 2). (d,e) Averaged normalized power spectral density of respiration (d) and mPFC LFP (e) across states as in (c). (f) Frequency-resolved comodulation of respiration and mPFC LFP oscillation power, across mice and behaviors (N = 9 mice). (g) Example coherence spectrum between respiration and mPFC LFP during offline states. Inset, average coherence value in the 2-5 Hz band (N = 9

mice). (h) Phase shift of 2-5 Hz filtered respiration and mPFC LFP signals during offline states for an example animal (blue histogram) and overlaid magnitude of phase modulation ($\log Z$) and average phase shift for all animals (red dots; $N = 9$ mice). Black arrow depicts the average phase and $\log Z$ of the phase shift for the example and the red arrow for the population. (i) Example spectral Granger causality between respiration and mPFC LFP for both causal directions. Inset, group statistics of the average Granger causality for the 4 Hz band (2–5 Hz) between respiration and mPFC LFP for both causality directions ($N = 9$ mice, Wilcoxon signed-rank test, resp ! mPFC versus mPFC ! resp, ** $P < 0.01$). a.u., arbitrary units; s.d., standard deviations. Shaded areas, mean \pm SEM.

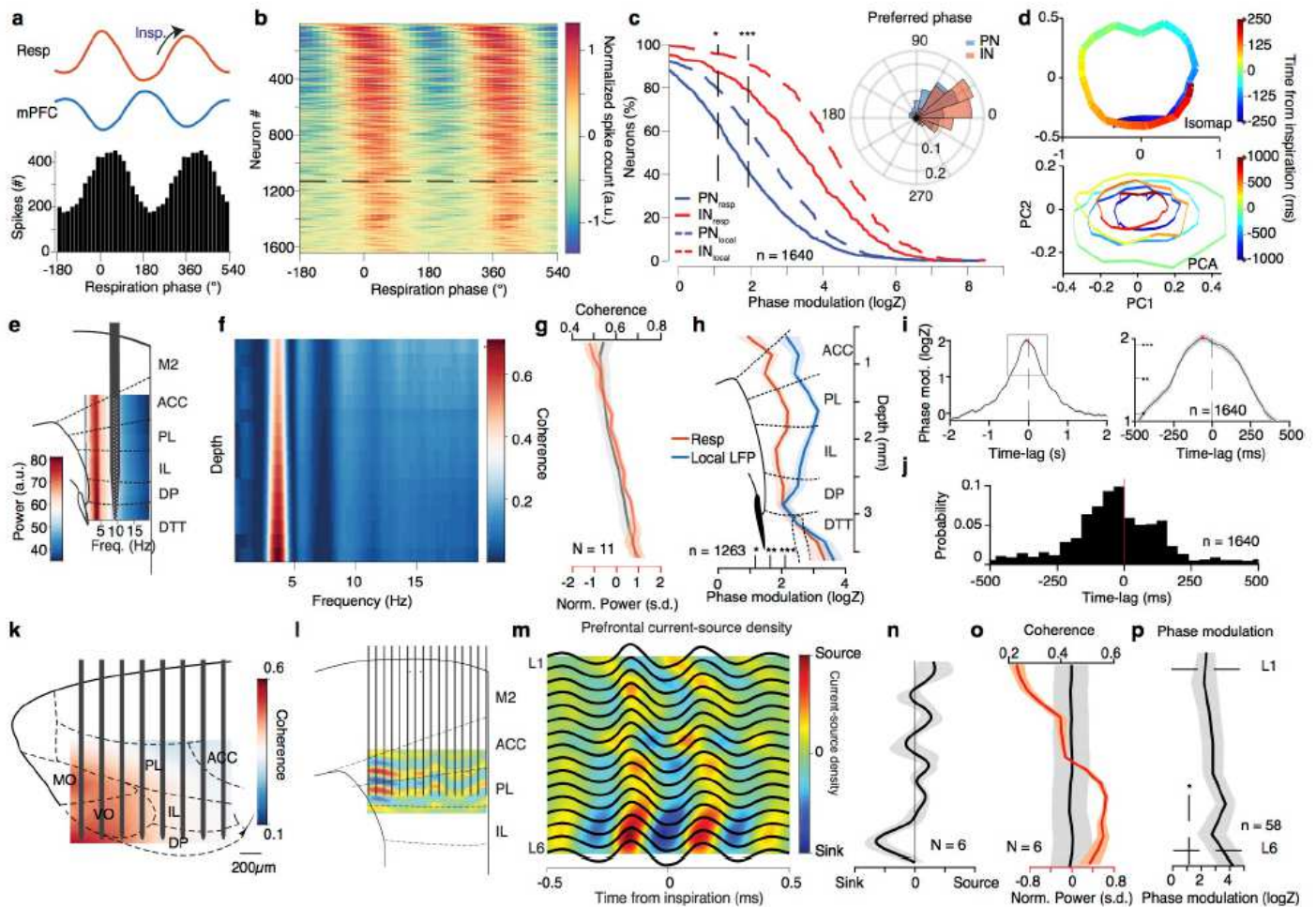


Figure 2

Topography of prefrontal circuit 60 entrainment by breathing. (a) Respiration phase histogram of the spiking activity of an example prefrontal neuron. Top, associated average respiration (red) and mPFC LFP (blue) traces. (b) Color-coded normalized phase histograms of all prefrontal neurons during offline states, ordered by phase modulation magnitude ($n = 1640$ neurons, $N = 13$ freely-behaving and head-fixed mice). The horizontal dashed line indicates the significance threshold for the $\log Z$. (c) Cumulative distribution of the $\log Z$ for all prefrontal PNs (blue, $n = 1250$ neurons) and INs (red, $n = 390$ neurons). Phase modulation is assessed in relation to the respiration (solid lines) and the local prefrontal LFP (dashed lines) (See also Supplementary Fig. 3). Inset: Distribution of the preferred phase for PNs (blue) and INs (red). The height

of each bar corresponds to the relative number of units. (d) Example trajectory of the mPFC neuronal population activity triggered on the inspiration onset as calculated using Isomap (top) and PCA (bottom) for a longer time window. (e) Schematic depiction of a typical recording using a high-density silicon polytrode inserted in the deep layers of the mPFC, overlaid on an example depth- and frequency-resolved power spectrum spanning all medial prefrontal subregions. (f) Example depth- and frequency-resolved coherence between the respiration and local prefrontal LFP spanning all medial prefrontal subregions. (g) Average depth-resolved normalized power (red) and coherence in the 2-5 Hz band (black) (N = 11 head-fixed mice). (h) Depth-resolved average phase modulation statistics ($\log Z$) (n = 1263 cells, N = 11 mice). (i) Time-lagged phase modulation of prefrontal neuronal population, indicative of directionality from respiration to prefrontal unit activity. Right, the magnified period marked with square. Red stars mark the peak lag (t = -65ms). Horizontal lines indicate levels of significant phase modulation. (j) Distribution of time lag of maximum phase modulation for the population of prefrontal neurons (n = 1640 neurons, N = 13 mice). (k) Example of 2D coherence between respiration and local LFP throughout the frontal subregions. (l) Schematic depiction of a 16-shank probe (50 μ m shank spacing) inserted in the prelimbic region of the mPFC to record simultaneously from all cortical layers and an example inspiration-triggered current-source density profile. (m) Example average inspiration-triggered LFP traces and overlaid corresponding translaminar current-source density profile from the dorsal mPFC. (n) Average inspiration-triggered translaminar normalized current-source density profile from the dorsal mPFC (N = 6 head-fixed mice). (o) Average cortical layer-resolved profile of the normalized 2-5 Hz band local LFP power (red) and coherence with respiration (coherence) (N = 6 mice). (p) Cortical layer-resolved unit phase modulation statistics ($\log Z$) (n = 58 cells, N = 6 mice). Shaded areas, mean \pm SEM, a.u., arbitrary units; s.d., standard deviations; L1, layer 1; L6, layer 6. Stars indicate significance levels (* P<0.05; ** P<0.01; *** P<0.001).

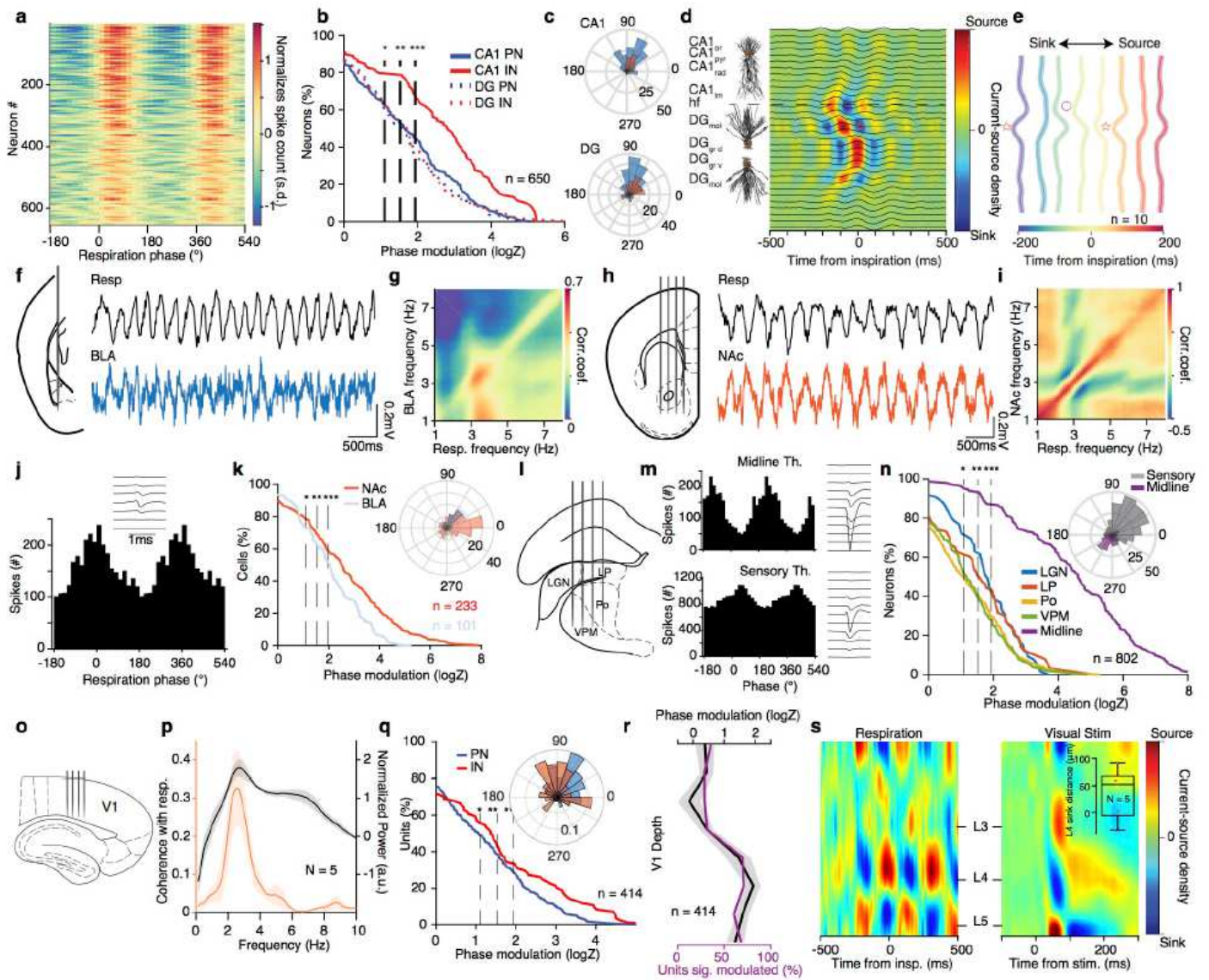


Figure 3

Breathing modulates hippocampal, thalamic, BLA, NAc, 155 and V1 neuronal activity. (a) Color-coded respiration phase histograms of the normalized firing rate of all hippocampal cells ($n = 650$ cells). (b) Cumulative distribution of the modulation strength by respiration phase for all CA1 and DG PNs (CA1, $n = 226$ cells; DG, $n = 206$ cells; $N = 22$ mice) and INs (CA1, $n = 98$ cells; DG, $n = 120$ cells). (c) Distribution of the preferred phase for all significantly phase-modulated CA1 (top) and DG (bottom) cells. (d) Schematic depiction of CA1 pyramidal and DG granular cell somatodendritic domains aligned to the example inspiration-triggered high-density CSD profile of the dorsal hippocampus. Horizontal dashed line indicates the hippocampal fissure (See also Supplementary Fig. 5 for interpretation). (e) Average normalized inspiration-triggered CSD profile of dorsal hippocampus at different lags from inspiration ($N = 10$ head-fixed mice). Stars mark the middle molecular layer sink and circles the outer molecular layer sink (f, h) Left, schematic of recording configurations. Right, example simultaneously recorded respiration and BLA (f) or NAc (h) LFP trace. (g, i) Example frequency-resolved comodulation of respiration and BLA (g) or NAc (i) LFP oscillation power. (j) Respiration phase histogram of the spiking activity of one example NAc

neuron. Inset, the spatio-temporal spike waveform for the respective units. (k) Cumulative distribution of the logZ for all BLA (blue) or NAc (red) cells (BLA: n = 101 cells, NAc: n = 233 cells). Inset, distribution of the mean preferred respiration phases of all significantly modulated cells. (l) Schematic of recording configuration for sensory thalamus. (m) Respiration phase histograms of the spiking activity (left) and spatio-temporal spike waveforms of respective example units from the midline (top) and sensory (bottom) thalamus. (n) Cumulative distribution of the modulation strength for all thalamic neurons (n=802 cells). Inset, distribution of the preferred phase for all significantly phase-modulated sensory and midline thalamic cells. (o) Schematic of recording configuration for V1. (p) Spectral V1 LFP power and coherence with respiration. (q) Cumulative distribution of the modulation strength by the respiration phase for all V1 PNs and INs. Inset, distribution of the preferred respiration phase for all significantly phase modulated neurons. (r) Cortical depth-resolved phase modulation magnitude and cell percentage. (s) Example inspiration-triggered high-density CSD profile of V1, compared with the CSD profile triggered on visual stimulation. Inset, spatial distance between L4 sinks for respiration and visual stimulation-triggered CSD. Stars indicate significant phase modulation levels (* P<0.05; ** P<0.01; *** P<0.001).

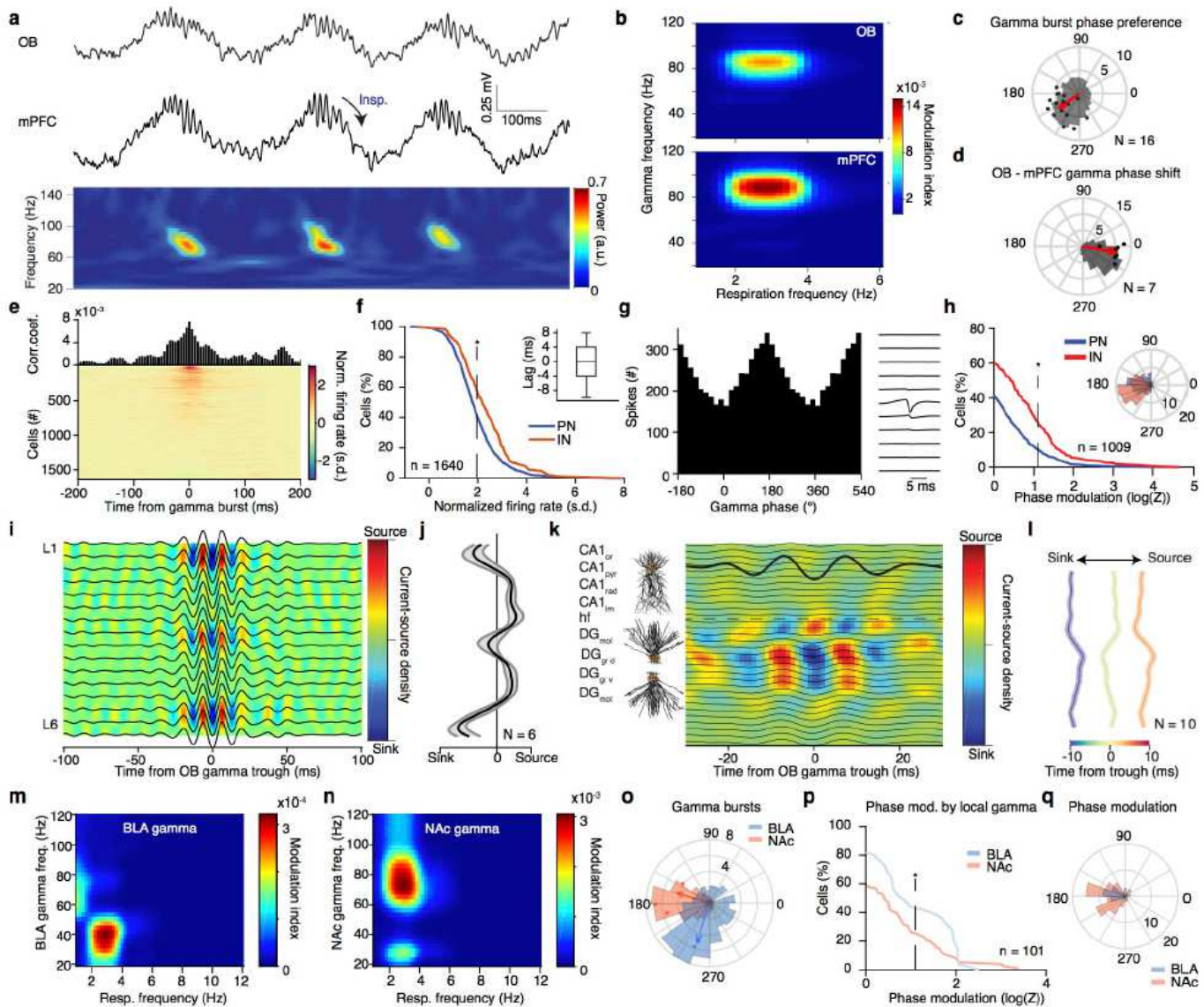


Figure 4

Reafferent gamma entrainment 204 of limbic circuits. (A) Example simultaneously recorded LFP traces (top) from OB and mPFC LFP and the spectral decomposition of mPFC LFP in the gamma range (bottom). (b) Color-coded modulation strength of OB (top) and mPFC (bottom) gamma power by respiration phase for an example animal. (c) Phase distribution of mPFC gamma bursts for an example animal (gray histogram) and average preferred phase and phase modulation strength ($\log Z$) for all animals ($N = 16$ freely-behaving and head-fixed mice). The red arrow indicates the population average preferred phase and $\log Z$. (d) Distribution of the phase shift between OB and mPFC gamma filtered traces for one example animal (gray histogram) and average phase shift and phase-coupling strength ($\log Z$, red dots) for all animals ($N = 7$ mice) (See also Supplementary Fig. 6). (e) Gamma-burst triggered time histogram for one example mPFC cell and color-coded normalized time histograms for all mPFC cells ($n = 1640$ cells). (f) Cumulative distribution of the gamma-triggered normalized firing of mPFC PNs ($n = 1250$ cells) and INs ($n = 390$ cells). Inset, time-lag between time from gamma burst and peak firing probability for all significantly responsive cells. (g) Gamma phase histogram of one example mPFC unit (left) and the respective unit spike spatio-temporal waveform (right). (h) Cumulative distribution of the modulation strength ($\log Z$) for all PNs (blue, $n = 685$ neurons) and INs (red, $n = 324$ neurons). Phase modulation is assessed in relation to the phase of the locally recorded prefrontal gamma oscillation. Inset, distribution of the mean preferred phases of all significantly modulated PN and IN cells. (i, j) Example (i) and average zero-lag (j) OB gamma-triggered translaminar CSD of the dorsal mPFC LFP profile. ($N = 6$ head-fixed mice). (k) Example OB gamma-triggered CSD profile of dorsal hippocampus. Horizontal dashed line indicates the hippocampal fissure. (l) Average normalized OB-triggered current-source density profile of the dorsal hippocampus at different time lags from OB gamma trough ($N = 10$ head-fixed mice). (m, n) Example phase-power modulation of BLA (m) and NAc (n) gamma activity by respiration. (o) Example distribution of the respiratory phase of BLA and NAc gamma bursts (histogram) and mean preferred phase of gamma occurrence and modulation strength (dots; BLA, blue, $N = 3$ head-fixed mice; NAc, red, $N = 4$ head-fixed mice). (p) Cumulative distribution of modulation strength for local gamma phase entrainment of spikes of all BLA (blue, $n = 25$ cells) and NAc cells (red, $n = 76$ cells). (q) Distribution of the mean preferred gamma phase for each significantly modulated BLA and NAc cell. Star indicates significance ($* P < 0.05$). Shaded areas, mean \pm SEM.

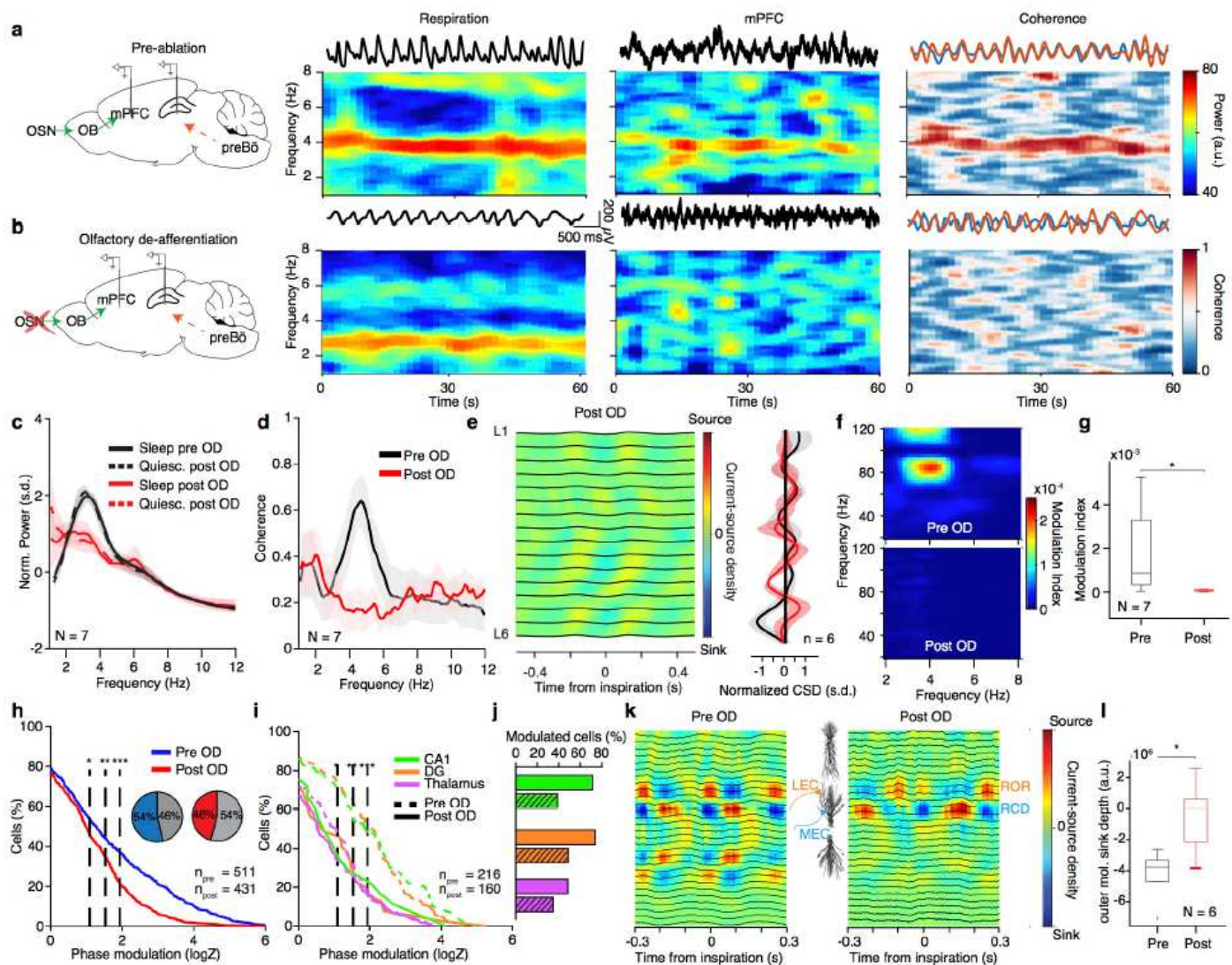


Figure 5

Reafferent respiratory input accounts for LFP but not neuronal entrainment. (a,b) Left, schematic of the manipulation strategy. Right, example time-frequency decomposition of power and coherence between respiratory and mPFC LFP signals during quiescence before (a) and after (b) OD. (c) Average normalized mPFC power spectra before and after OD (N = 7 head-fixed mice). (d) Coherence spectrum between respiration and mPFC LFP before and after OD (N = 7 mice). (e) Left, example inspiration-triggered CSD of the mPFC LFP during quiescence and sleep after OD. Right, average normalized CSD at zero lag (N = 6 mice) (See also Supplementary Fig. 7). (f) Example power-phase modulation of mPFC gamma oscillations before (top) and after (bottom) OD. (g) Average mPFC power-phase modulation strength of ≈ 80 Hz gamma oscillations (N = 7 mice; paired t-test: before vs. after OD). (h) Cumulative distribution of modulation strength for all mPFC neurons pre and post OD (Pre: n = 511 cells; Post: n = 431 cells). Inset, percentage of significantly phase-modulated cells before and after OD. (i) Cumulative distribution of modulation strength for CA1, DG, and somatic thalamus neurons before and after OD. (j) Percentage of significantly phase-modulated cells before and after OD. (k) Example inspiration-triggered CSD of the dorsal hippocampus LFP before (left) and after (right) OD. (l) Average outer molecular layer sink depth (N

= 6 head-fixed mice; paired t-test: before vs. after OD). Shaded areas, mean \pm SEM a.u., arbitrary units; s.d., standard deviations; n.s., not significant. Shaded areas, mean \pm SEM. Stars indicate significance levels (* $P < 0.05$; ** $P < 0.01$; *** $P < 0.001$). s.d., standard deviations; a.u., arbitrary units; OD, olfactory deafferentation.

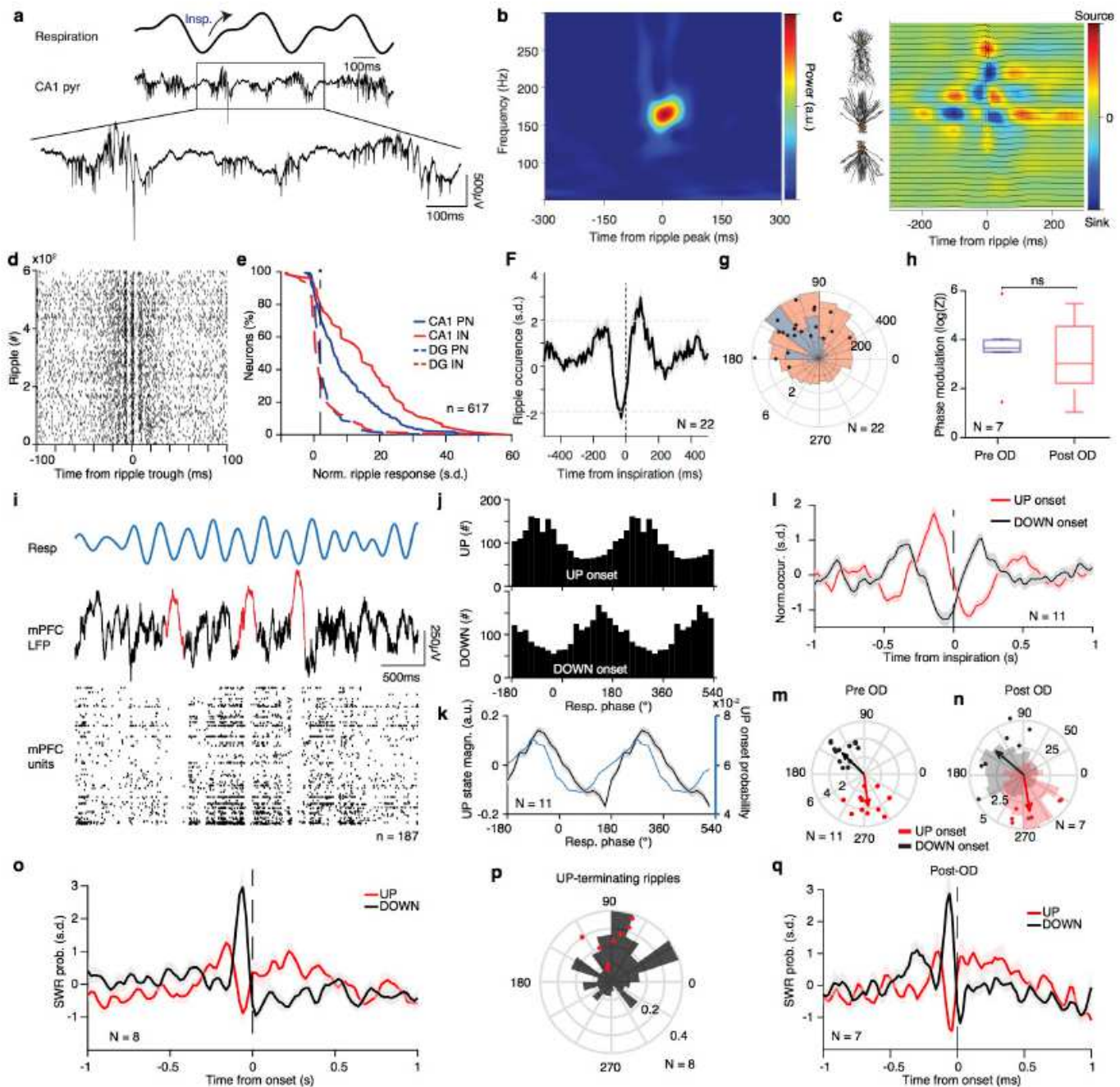


Figure 6

Breathing modulates hippocampal ripples and cortical UP states. (a) Example traces of the respiratory signal and CA1 pyramidal layer LFP. In the magnified LFP signal, ripple events and the associated spiking activity can be observed. (b) Average ripple-triggered time-frequency wavelet spectrogram of the CA1 pyramidal layer LFP from one example animal. (c) Schematic of the CA1 pyramidal and granular cells

somatodendritic domains aligned to the average ripple-triggered CSD profile of the hippocampal LFP activity for one example animal (See also Supplementary Fig. 8). (d) Ripple-triggered spike train of an example dCA1 neuron exhibiting evoked response and a characteristic oscillatory firing pattern. (e) Cumulative distribution of the ripple-triggered normalized firing of CA1 and DG PNs (CA1, n = 220 cells; DG, n = 202 cells) and INs (CA1, n = 76 cells; DG, n = 119 cells). (f) Average cross-correlation between inspiratory events and ripple occurrence (N = 22 freely-behaving and head-fixed mice). Dashed horizontal lines indicate the significance levels. (g) Distribution of the respiratory phase of occurrence of individual ripple events for one example animal (red; n = 4813 ripples) and preferred phase distribution for the population (blue; N = 22 mice). Overlaid, distribution of average phase and modulation strength for ripples (black dots). (h) Phase modulation of ripples before and after OD. (i) Example traces of respiration signal (top), mPFC LFP (middle trace), and spike trains of 187 simultaneously recorded mPFC units during sleep. Three typical delta waves and the corresponding DOWN states of the neuronal population are marked with red. (j) Example distributions of the breathing phase of UP (top) and DOWN (bottom) state onsets. (k) Normalized power (black) and occurrence probability (blue) for prefrontal UP states (N = 11 freely-behaving and head-fixed mice). (l) Cross-correlation of UP and DOWN state onsets with respect to inspiration. (m, n) Distribution of preferred breathing phase and phase modulation magnitude ($\log Z$) of UP and DOWN states before (m) and after (n) OD. (pre: N = 11 mice, post: N = 7 mice). Histogram in (n) is for one example session (scale is count of UP/DOWN states). (o) Probability of SWR occurrence as a function of time from UP or DOWN state onset (N = 8 mice). (p) Example (black) and distribution of preferred breathing phase of SWR occurrence, for SWRs that are terminating an UP state (red dots, N = 8 mice). (q) Probability of SWR occurrence as a function of time from UP or DOWN state onset after OD (N = 7 mice). Note that the observed pattern is identical to pre-OD shown in (o). s.d., standard deviations; a.u., arbitrary units; n.s., not significant; OD, olfactory deafferentation. Shaded areas, mean \pm SEM. Stars indicate significance levels (* $P < 0.05$; ** $P < 0.01$; *** $P < 0.001$).

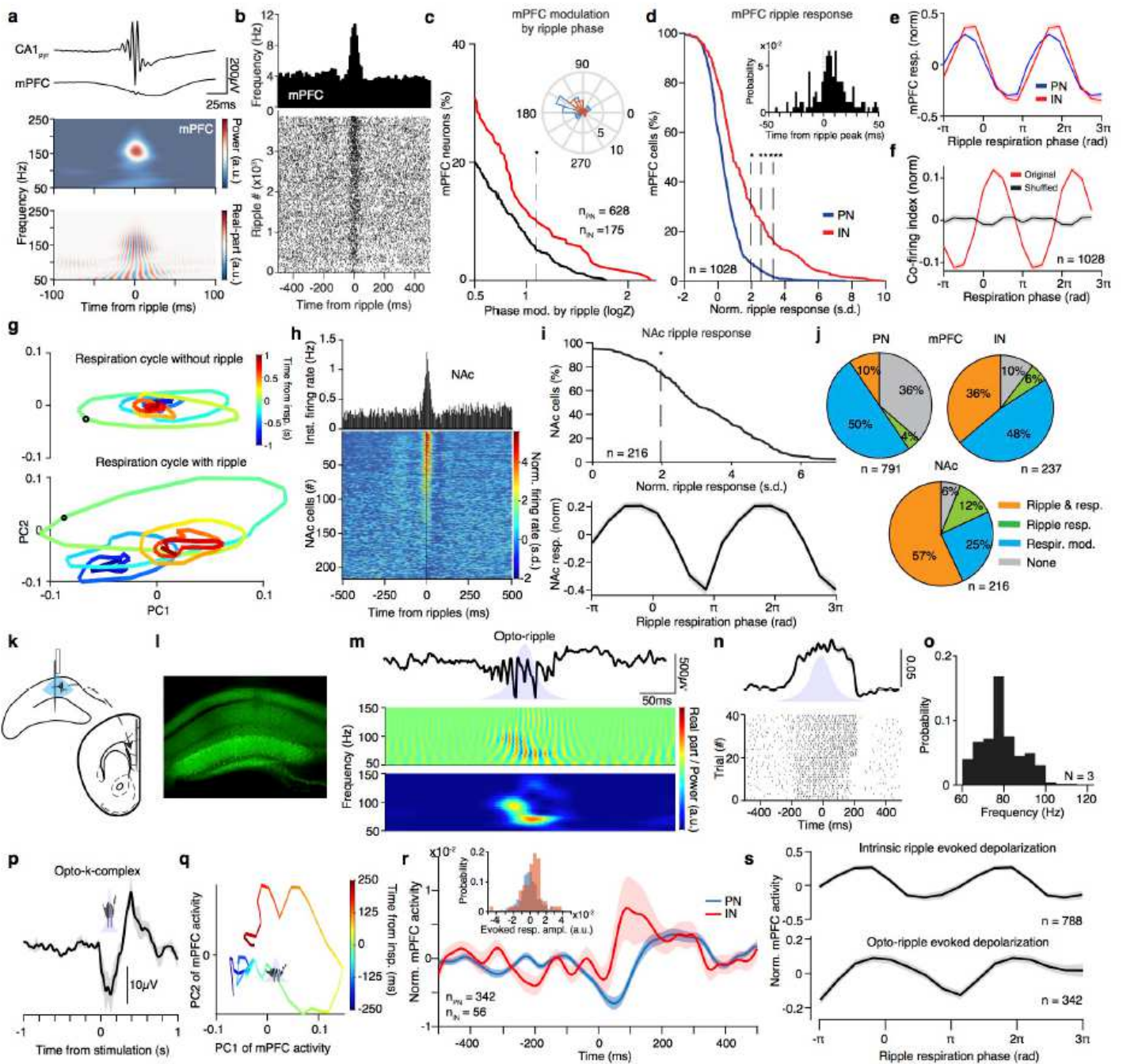


Figure 7

Breathing modulates the cortico-hippocampal 333 interaction. (a) Example average ripple-triggered CA1_{pyr} and mPFC LFP traces and wavelet spectral decomposition of mPFC LFP power (upper) and real-part (lower) ($n = 3162$ ripples). (b) Example mPFC unit spiking raster across individual ripples (bottom) and cross-correlogram of unit firing to ripple (top). (c) Cumulative distribution of the modulation strength by the phase of the hippocampal CA1 ripple oscillation for all mPFC PNs ($n = 628$ cells) and INs ($n = 175$ cells). Inset, distribution of the preferred phase for all significantly phase-modulated cells. (d) Cumulative distribution of the ripple-triggered normalized firing of mPFC PNs ($n = 791$ cells) and INs ($n = 237$ cells) in response to ripples ($N = 11$ freely-behaving and head-fixed mice). Inset, distribution of time of unit firing

peak from time of ripple peak. (e) Prefrontal ripple-evoked response for PN (blue traces) and IN (red traces), as a function of the breathing phase of occurrence of ripple. (f) Average normalized co-firing index for all pairs of dCA1 and mPFC cells ($n = 14412$, $N = 13$ mice) compared to shuffle control. (g) Example trajectory of the mPFC population rate dynamics around the time of inspiration without (top) and with (bottom) a ripple oscillation occurring during that period in the oscillation. Black circle denotes time 0, pseudocolor codes for time from inspiration onset. (h) Cross-correlation of firing with respect to ripple time for one example NAc unit (top) and color-coded cross-correlograms for all NAc cells ($n = 216$ cells). (i) Top, cumulative distribution of the ripple-triggered normalized firing of NAc cells ($n = 216$ cells) in response to ripples ($N = 4$ mice). Bottom, ripple-evoked response as a function of the breathing phase of occurrence of ripple. (j) Top, pie charts indicating the percentage of all mPFC PNs (left; $n = 791$ cells) and INs (right; $n = 237$ cells) that are either phase modulated by respiration (resp. mod), responding significantly to ripples (ripple resp.), being both significantly modulated by breathing and significantly responsive to ripples or neither. Bottom, similarly, for all NAc cells ($n = 216$ cells). (k) Schematic of the experimental design for testing the effect of optogenetically induced hippocampal ripples on the prefrontal network. (l) Example histological reconstruction of the opsin expression in the dorsal hippocampus. (m) Example trace (top) and wavelet real part (middle) and power (bottom) of the oscillation generated in the dCA1 pyramidal layer during the optogenetic stimulation. Note the similarity with ripple oscillations. (n) Cross-correlation of firing with respect to optogenetic stimulation for one example dCA1 neuron and raster-plot for all events. (o) Probability distribution of the frequency of evoked oscillations during light stimulation. (p) Example average evoked response in the mPFC LFP triggered on the opto-ripple generation in the dCA1. (q) Example trajectory of the mPFC population around the time of inspiration when an opto-ripple is generated during inspiration. (r) Evoked response in the mPFC neuronal population triggered on the opto-ripple generation in the dCA1. Inset, distribution of the evoked response amplitude for all cells. (s) Normalized prefrontal neuron evoked activity to intrinsic (top) and optogenetically-generated (bottom) ripples, as a function of the respiratory phase of occurrence of the ripple. Shaded areas, mean \pm SEM, s.d., standard deviations; a.u., arbitrary units; FR, firing rate. Stars indicate significance levels (* $P < 0.05$; ** $P < 0.01$; *** $P < 0.001$).

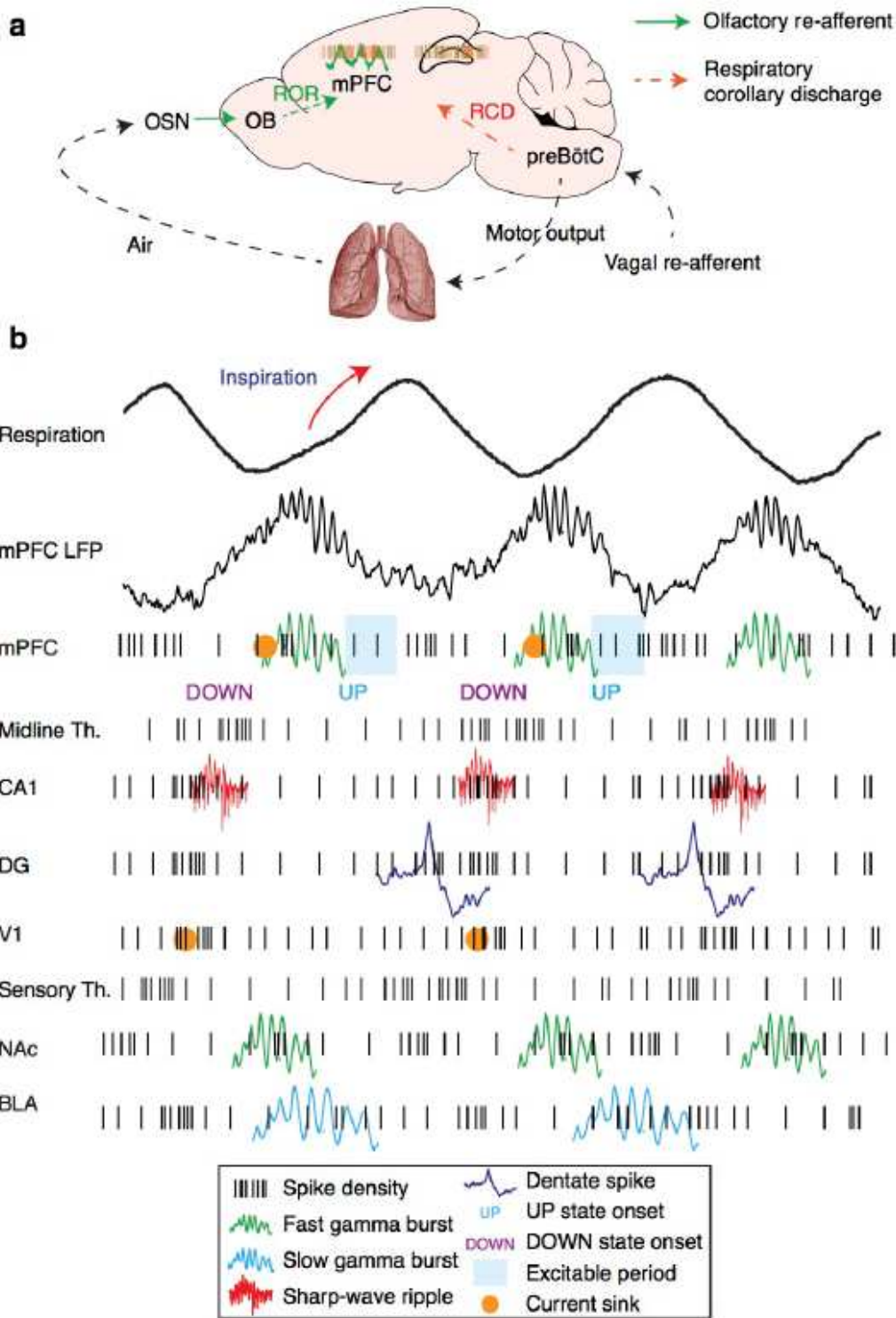


Figure 8

Breathing organizes network dynamics across limbic structures. (a) Schematic depiction of the efferent copy pathway carrying the respiratory corollary discharge (RCD) signal and the reafferent pathway carrying the respiratory olfactory reafferent (ROR) signal. (b) Summary schematic of the network dynamics organized by breathing throughout all structures studied. Black traces: LFPs; Black ticks: neuronal spikes; Green traces: Fast (≈ 80 Hz) gamma; Cyan traces: Slow gamma (≈ 40 Hz); Red traces: CA1

Ripples; Blue traces: Dentate spikes; Orange dots: CSD sinks (mPFC deep layers, V1 LGN input, and DG middle molecular layer); Blue shadow: Cortical excitability period.

Supplementary Files

This is a list of supplementary files associated with this preprint. Click to download.

- [Karalis2021NatureCommSupplFigures.pdf](#)